Asteroseismic modelling of mild Am δ Sct stars : HD 13038 and HD 13079

Mrinmoy Sarkar [1,2], Santosh Joshi[1], Marc-Antoine Dupret[3], Gaël Buldgen [3], Athul Dileep [1], Peter De Cat [4], Surath C. Ghosh [1] and Archana Gupta[2]
[1]Aryabhatta Research Institute of Observational Sciences, Manora Peak, Nainital-263002, India
[2]Department of Applied Physics, M.J.P. Rohilkhand University, Bareilly, Uttar Pradesh, 263006, India
[3]Space Sciences, Technologies and Astrophysics Research (STAR) Institute, University of Liège, B-4000 Sart Tilman, Belgium
[4]Royal Observatory of Belgium, Ringlaan 3, B-1180 Brussels, Belgium

Accepted XXX. Received YYY; in original form ZZZ

ABSTRACT

In this paper, we present an asteroseismic analysis of two mild Am δ Sct (δ Sct) pulsators, HD 13038 and HD 13079, utilising both the space and ground-based photometry. From multi-sector *TESS* observations with different cadences, 37 pulsation frequencies for HD 13038 and 69 for HD 13079 were extracted with SNR > 5. Notably, light curves of HD 13079 are affected by ∼ 15% of the flux from its neighbourhood star HD 13079B situated at an angular separation of 6.48 ± 2.70 *arcsec*. For HD 13038, the large frequency separation ($\Delta\nu$) is 6.08 d^{-1} leading two vertical ridges of radial modes consistent with the frequency ratios and pulsation constants (Q-value). However, the seismic age indicates the left-ridge frequencies are more acceptable as radial modes with orders $n = 5, 7$. We found that one radial ridge is visible for HD 13079 at $\Delta\nu = 5.15$ d^{-1} with orders $n = 1, 2, 3, 4, 6$. For both stars, excited radial overtones are higher than the predicted values for these $T_{\rm eff}$ range. The stellar parameters were calculated using a mass-metallicity (M–Z) grid followed by seismic-χ^2 minimisation technique constraining identified radial modes. The possible rotation frequencies for HD 13038 and HD 13079 are found at 0.94 d^{-1} and 0.86 d^{-1}, provides inclination angle of ∼ 90° and ∼ 42° respectively. The present study is a crucial step in comprehending the processes that underlie the excitation of high-order radial modes in Am stars.

Key words: Asteroseismology – Am Star – δ Sct pulsations – individual: HD 13038 – individual: HD 13079 – Stellar Rotation – Quintuplets

1 INTRODUCTION

Asteroseismology, the study of stellar pulsations identified as periodic variations of surface brightness, radial velocities (RV) and/or line profile variations, is employed to probe the internal structures and evolution of stars. Analysing the frequencies of pressure (p), gravity (g), and mixed modes provides valuable information on the stellar interiors, including core nucleosynthesis processes, composition gradients, and internal rotation (Aerts et al. 2010). Space-based missions like as *Kepler* and *TESS* have revolutionized the research field by facilitating high-precision observations across a wide range of spectral types including intermediate-mass pulsators (Hall et al. 2022; Theodoridis & Tayar 2025). Comparisons between observed pulsation frequencies and theoretical models impose strong constraints on the stellar parameters such as mass, age, and internal mixing, thereby enhancing the knowledge of stellar evolution (Rendle et al. 2019; Wang et al. 2023; Panda et al. 2024).

The δ Sct stars are a class of short-period pulsating variables characterised by spectral types A and F and located in the bottom region of the classical instability strip which intersects the main-sequence (MS). Their masses range from 1.5 to 2.5 $M_\odot$ where pulsation of low-order radial and non-radial p-modes are excited with periods spanning from 0.01 to 0.3 days. The pulsations in these stars are driven by the κ-mechanism operating in the second helium ionisation zone (Aerts et al. 2010; Chang et al. 2013; Martinez-Vazquez et al. 2023). The high-precision photometry from *Kepler* and *TESS* has demonstrated that numerous δ Sct stars display complex frequency spectra (Bedding et al. 2020). Some of the δ Sct stars exhibit pulsation frequencies in both the low ($\nu < 5$ d^{-1}) and high ($\nu > 5$ d^{-1}) frequency ranges. They are known as hybrid pulsators and are important test beds to probe the envelope and deep interiors, simultaneously (Balona 2016a; Guzik et al. 2022).

The metallic-lined A-type (Am) stars constitute a category of chemically peculiar (CP) stars distinguished by enhanced absorption lines of iron-peak and rare-earth elements (e.g. Zn, Sr, Zr, Ba) alongside under-abundances of Ca and Sc (Boiarchuk & Savanov 1986; Savanov 1995, 1998; Saffe et al. 2020). These abundance patterns are described by atomic diffusion processes where radiative levitation and gravitational settling operate efficiently in the absence of significant turbulence (Michaud 1970a; Boiarchuk & Savanov 1986). The Am stars typically exhibit slow rotation, a property that is largely explained by tidal synchronization in close binary systems (Abt & Levy 1985; Abt 1961; Michaud 1970b; Preston 1974; Hauck & North 1993), where tidal forces brake the stellar rotation and keep it synchronized with the orbital motion. This low rotational velocity facilitates the efficient operation of atomic diffusion mechanisms in their atmospheres (Monaghan 1970; Iliev & Budaj 2008). Historically, Am stars were not expected to pulsate, as settling of helium inhibits the operation of κ-mechanism. Nonetheless, recent studies have shown that a considerable fraction of Am stars do exhibit δ Sct-

type pulsations, particularly those located near the red edge of the instability strip (Smalley et al. 2017; Dürfeldt-Pedros et al. 2024).

Asteroseismic modelling of δ Sct stars entails constraining observed pulsation frequencies with those predicted by stellar evolution and pulsation models to deduce their internal structures (Aerts et al. 2010). These stars are ideally suited for asteroseismology as their low-order p-modes are sensitive to the outer stellar layers, while in some cases, mixed modes can probe deeper regions (Joshi & Joshi 2015). However, mode identification poses challenges due to the dense and often irregular frequency spectra, especially at moderate rotation rates (Murphy et al. 2019). A comparison of the observed radial modes along with the model frequencies can constraint the evolutionary models within the H-R diagram (Sarkar et al. 2024b).

To address the cited issues, advanced modelling employs grids of evolutionary models utilizing adiabatic pulsation codes (Christensen-Dalsgaard 2008; Paxton et al. 2013; Claret 2004). Observational diagnostics including frequency ratios, échelle diagrams, and Q-values are extensively used to identify the radial orders of the pulsation modes (Breger et al. 1999). This provides essential constraints on the stellar models, enabling precise measurements of fundamental stellar parameters such as mass, radius, core hydrogen abundance, and metallicity (Nsamba et al. 2021; Kallinger et al. 2010).

Stellar rotation significantly influences the structure of the frequency spectra of the Am stars exhibiting δ Sct pulsations. In non-radial modes, rotation breaks the frequency degeneracy, producing multiplets through rotational splitting. The amplitude and symmetry of these splittings depend on the star's internal rotation profile and inclination angle (Reese et al. 2008; Bedding et al. 2020; Suárez et al. 2014). A recent study by Guo et al. (2024) showed that the rotational distortion in stars can produce asymmetry in the splitting of the non-radial modes. Many δ Sct stars have moderate to rapid rotation, and in favourable cases rotational splitting of pulsation modes can be detected. According to (Van Reeth et al. 2016), this splitting can be used to confine the internal rotation rate and hence provide insight into angular momentum transfer when clear mode identification is achievable. However, in many δ Sct stars, fast rotation, sparse mode spectra, and complex mode identification make rotational splitting difficult to measure unambiguously. The Am stars, typically characterized by slow rotation, often display less complex frequency spectra, hence aiding the mode identification. However, the same slow rotation can limit sensitivity to variable rotation within the interior, complicating to analysis of the angular momentum transport (Murphy 2014; Antoci et al. 2019).

2 SAMPLE SELECTION

The sample for the present study was selected from the catalogue of the Nainital-Cape (N-C) survey project, which commenced approximately three decades ago at the Aryabhatta Research Institute of Observational Sciences (ARIES) and the South African Astronomical Observatory (SAAO) in collaboration with the Indian Space Research Organization (ISRO), Bengaluru, India. The primary aim of this survey was to search for and study new rapidly oscillating Ap (roAp) stars in the Northern and Southern hemispheres.

During the survey, rapid oscillations were discovered in one of the Ap stars (HD 12098; Girish et al. 2001) while δ Sct-type pulsations were detected in seven Am stars (HD 13038, HD 13079, HD 25515, HD 98851, HD 102480, HD 113878, and HD 118660; Martinez et al. 2001a; Joshi et al. 2003, 2006, 2009, 2010, 2012, 2016, 2017, 2022b, 2025). Dileep et al. (2024) revisited the N-C survey stars with *TESS* data and found that many of them exhibit pulsational and/or rotational variabilities. Recently, Dileep et al. (2025a,b) also investigated the impacts of contamination from adjacent stars, highlighting the importance of ground-based observations for distinguishing the pulsational signals of distinct components. Asteroseismic examinations were undertaken on the multi-periodic Am star HD 118660 by Sarkar et al. (2024a,b) and a detailed study of the remaining δ Sct stars discovered under the N-C survey is in progress. For our current study, we focus on two MS multi-periodic Am stars showing δ Sct-type pulsations, namely, HD 13038 and HD 13079. The fundamental parameters of these targets are listed in Table 1.

2.1 HD 13038 (TIC 374971192)

HD 13038 is classified as an A3-type star in the Henry Draper Catalogue (Hauck & Mermilliod 1998). According to the $uvby\beta$ photometric catalogue, the measured β index is 2.856, which corresponds to the early A-type spectral class. The dominant pulsation mode in HD 13038 exhibits a period of approximately 29 min ($\approx 49.6\, d^{-1}$), which was first detected using the ground-based photometric observations in the Johnson-B band by Martinez et al. (1999b). Subsequent investigation by Martinez et al. (2001b) detected additional pulsation frequencies at 0.58 mHz ($\approx 50.1 d^{-1}$) and 0.46 mHz ($\approx 39.7 d^{-1}$). Follow-up studies of non-local, time-dependent convection models show that the position of HD 13038 is slightly below the ZAMS in the H-R diagram (Xu et al. 2002).

Employing high-resolution spectroscopic and spectropolarimetric investigations, Joshi et al. (2017) reported the atmospheric parameters including the projected rotational velocity as $v \sin i = 87 \pm 5$ km s^{-1}. The iron abundance was determined to be [Fe/H] = 0.06 ± 0.19 relative to the solar value. Sodium and vanadium are markedly elevated, with [Na/H] = +0.98 and [V/H] = +1.64 while the heavy elements barium and cerium also display considerable overabundances: [Ba/H] = +0.87 and [Ce/H] = +0.68 in conjunction with the under-abundance of zinc [Zn/H] = −1.09 (Joshi et al. 2017). These parameters are indicative of a mild Am nature.

2.2 HD 13079 (TIC 184679514)

HD 13079 (also known as V419 And) is a double star system in which a pulsation period of 78 min ($\approx 18.4\, d^{-1}$) was discovered by Martinez et al. (1998, 1999a). An attempt to search for the presence of binary components was unsuccessful (Liakos & Niarchos 2017). According to the *Hipparcos* catalogue, the magnitudes of the primary (HD 13079) and secondary component (HD 13079B) are 8.989 ± 0.007 and 11.311 ± 0.057, respectively. Strömgren photometric indices suggest that the primary component (HD 13079) is a cool Am-type star (Martinez et al. 1999a).

Using high-resolution spectroscopy, Joshi et al. (2017) measured a projected rotational velocity of $v \sin i = 56 \pm 3$ km s^{-1} and a photospheric iron abundance of [Fe/H] = -0.18 ± 0.15, which is close to the solar value. They also found significant overabundances of heavy elements, in particular cerium (Ce) and samarium (Sm). Furthermore, their spectropolarimetric observations showed no detectable magnetic field, providing strong evidence that the star is a mild Am-type object.

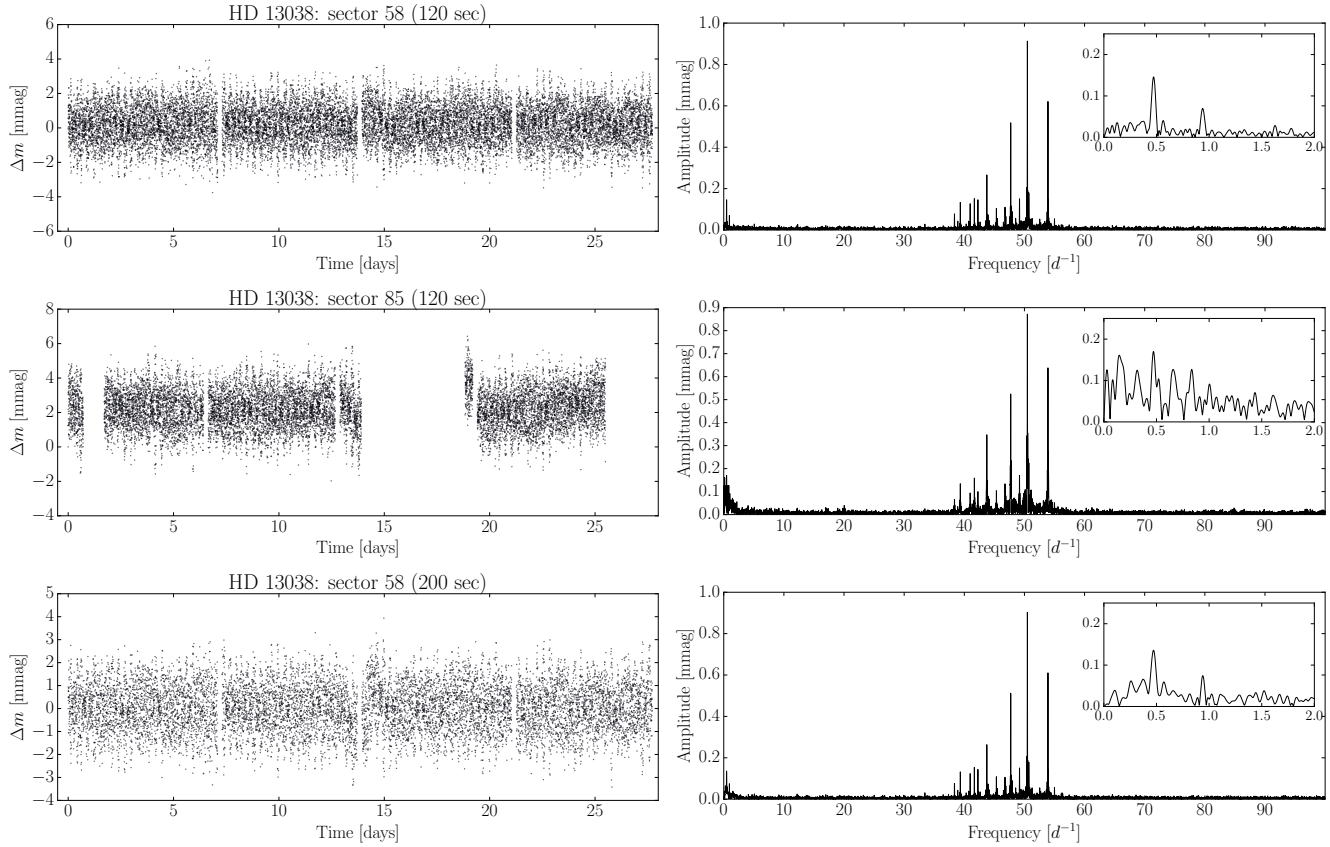

Figure 1. Left panels: Light curves of HD 13038 for the given sectors and cadences as marked in each panel. Right panels: The amplitude spectra of the corresponding time-series data shown in the left panels.

3 OBSERVATIONS AND DATA REDUCTION

3.1 Space-based Photometry

The high-precision photometric time-series data of the studied stars were obtained by the *Transiting Exoplanet Survey Satellite* (*TESS* Ricker et al. 2015). The data sets were downloaded from the *TESS* Science Processing Operations Centre (SPOC; Jenkins et al. 2016), which is accessible to the public at the Mikulski Archive for Space Telescopes (MAST). We utilised the Pre-search Data Conditioning Simple Aperture Photometry (PDCSAP) light curves, which employ co-trending basis vectors to alleviate instrumental systematics and long-term drifts (Twicken et al. 2010). The short-(180 *sec*, 200 *sec*) and long-cadence (1800 *sec*) PDCSAP fluxes were acquired utilising the LIGHTKURVE Python package (Lightkurve Collaboration et al. 2018). The *TESS* time-series are available for HD 13038 for sectors 58 and 85, while HD 13079 was observed in sectors 18 and 58. The left panels of Fig. 1 and Fig. 2 show light curves of HD 13038 and HD 13079 as observed in the multiple sectors.

Frequency spectra were produced with the PERIOD04 software package (Lenz & Breger 2005), which executes simultaneous multi-sine fitting and pre-whitening processes. Frequencies were identified using a signal-to-noise ratio threshold of $SNR > 5$ (Baran et al. 2015) with noise level calculated as the mean of the amplitude of the residual of the Fourier spectrum after the removal of dominating peaks. The Rayleigh resolution criterion, defined as $1.5/T$ (where T represents the temporal span of the data), was opted to evaluate frequency accuracy. The combined frequency spectra from all sectors of *TESS* data are utilised to compute the frequencies for increased resolution in the frequency spectra, as illustrated in Fig. 3 for both stars.

Table 1. Overview of the fundamental parameters of the targets, i.e. the *Gaia* DR3 parallax (π), the extinction (A_V), apparent magnitude (m_V), and absolute magnitude (M_V) in the V band, the distance (d), the effective temperature ($T_{\rm eff}$), the luminosity ($\log(L/L_\odot)$), the projected rotational velocity ($\upsilon \sin i$), and the radius (R) calculated using Stefan-Boltzmann law.

Parameter	HD 13038	HD 13079
π (mas)	6.085615	5.512474
A_V (mag)	0.31*	0.09*
m_V (mag)	8.52	8.90
M_V (mag)	2.106 ± 0.012	2.507 ± 0.009
d (pc)	166.23	181.40
$T_{\rm eff}$ (K)	7960 ± 200*	7040 ± 200*
$\log(L/L_\odot)$ (dex)	1.052 ± 0.005	0.889 ± 0.003
$\upsilon \sin i$ (km. s^{-1})	87 ± 5*	56 ± 3*
R ($R_\odot$)	1.765 ± 0.089	1.873 ± 0.107

*Joshi et al. (2017)

TESS possesses a rather coarse spatial resolution, with each pixel covering an angular dimension of around 21 *arcsec*; hence, numerous objects may reside within a single *TESS* pixel, leading to contamination in the light curve that can remain after careful masking procedures. A thorough investigation of the *TESS* pixel data is essential, especially when the target is situated in a dense populated field (Dileep et al. 2025a).

We used the contamination and aperture flux-loss metrics

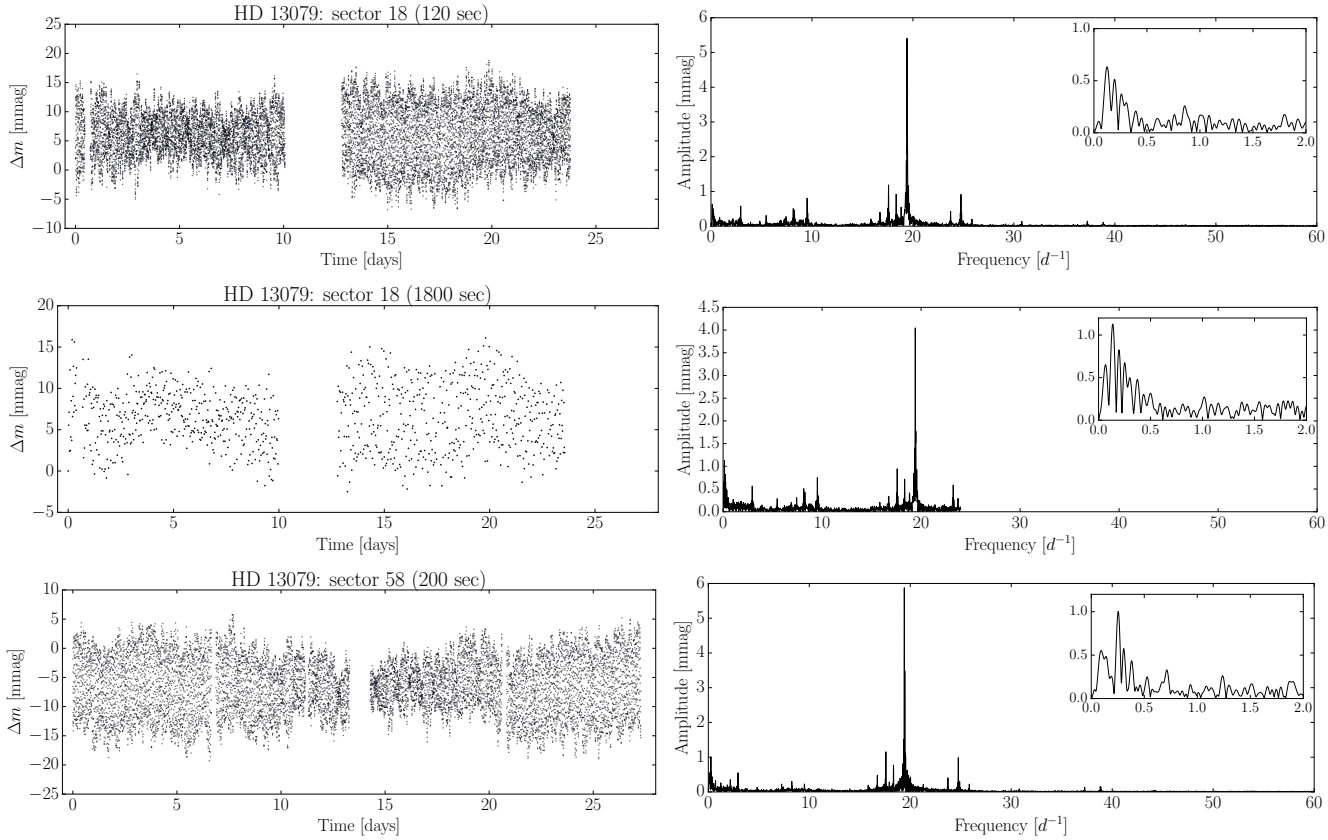

Figure 2. Same as Fig. 1 but for HD 13079.

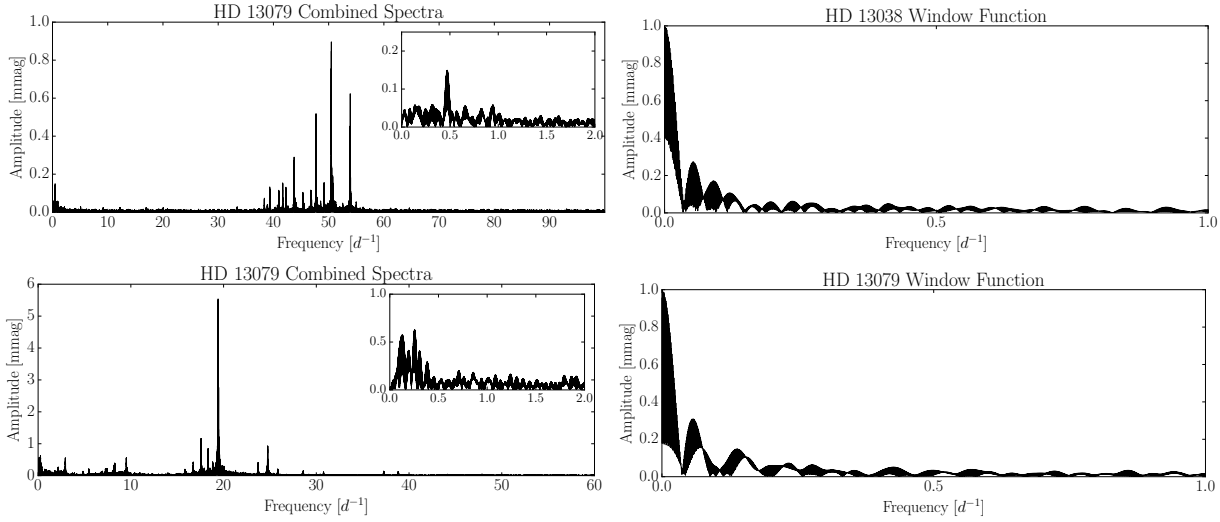

Figure 3. Combined frequency spectra of the *TESS* SPOC time-series data shown in the left panels of Figs. 1 and 2 for the targets HD 13038 (top left panel) and HD 13079 (bottom left panel). The inset plots in the left panels present a zoomed view of the frequency range $(0, 2)$. The corresponding window functions are displayed in the right panels.

CROWDSAP and FLFRCSAP provided by the SPOC pipeline (Ricker et al. 2015; Jenkins et al. 2016). Very low-contamination ($\approx 4\%$) was detected for HD 13038. However, HD 13079 exhibited a contamination level of $\approx 15\%$ due to its companion star HD 13079B, which is ≈ 2 mag fainter (in the G-band) than the primary component HD 13079. Fig 4 illustrates the *TESS* target pixel files (TPF) for HD 13038 (left) and HD 13079 (right) overlaid with *Gaia* DR3 sources in the field and their respective magnitude differences in the G-band.

It is noteworthy to mention here that the contaminating star, HD 13079B, has an effective temperature of approximately 5799 K, as calculated by the `GSP-Phot` module in *Gaia* DR3 (Andrae et al.

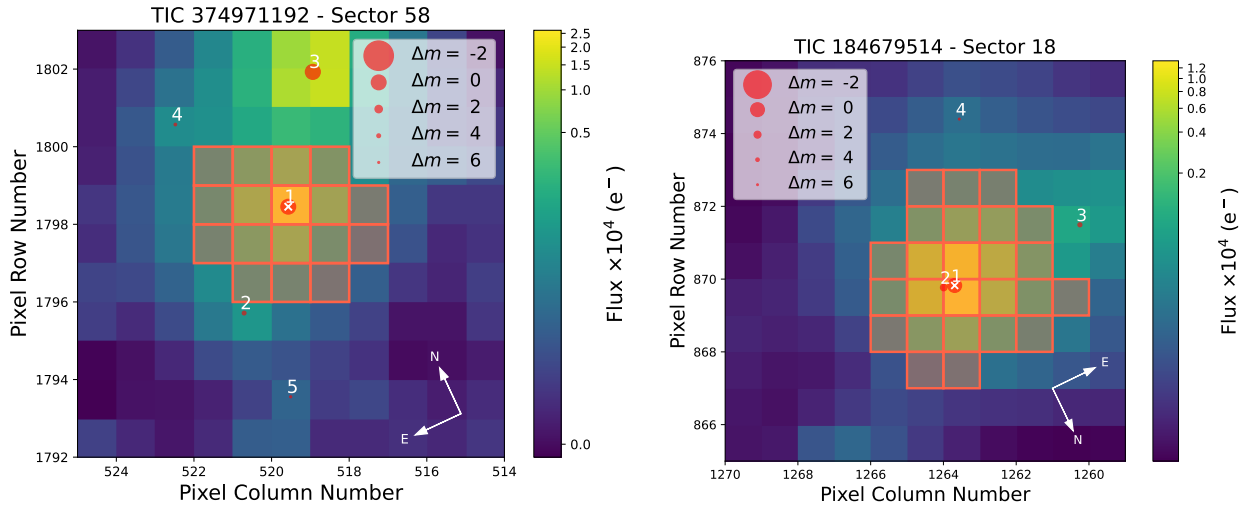

Figure 4. Identification of Gaia sources around the target exhibiting a magnitude difference of up to 6 are overlaid on the *TESS* pixels utilising `TPFplotter` (Aller et al. 2020). In the legend, the size of the circle denotes the brightness of the stars relative to the target with Δm = 0, labelled as numeral 1. The pipeline aperture applied to the light curves is indicated with red boxes. The left panel indicates that none of the sources are within the aperture, and no notable contamination is observed. In the right panel, the source number 2 is located within the pipeline aperture of source 1 with a contamination level of ≈ 15%.

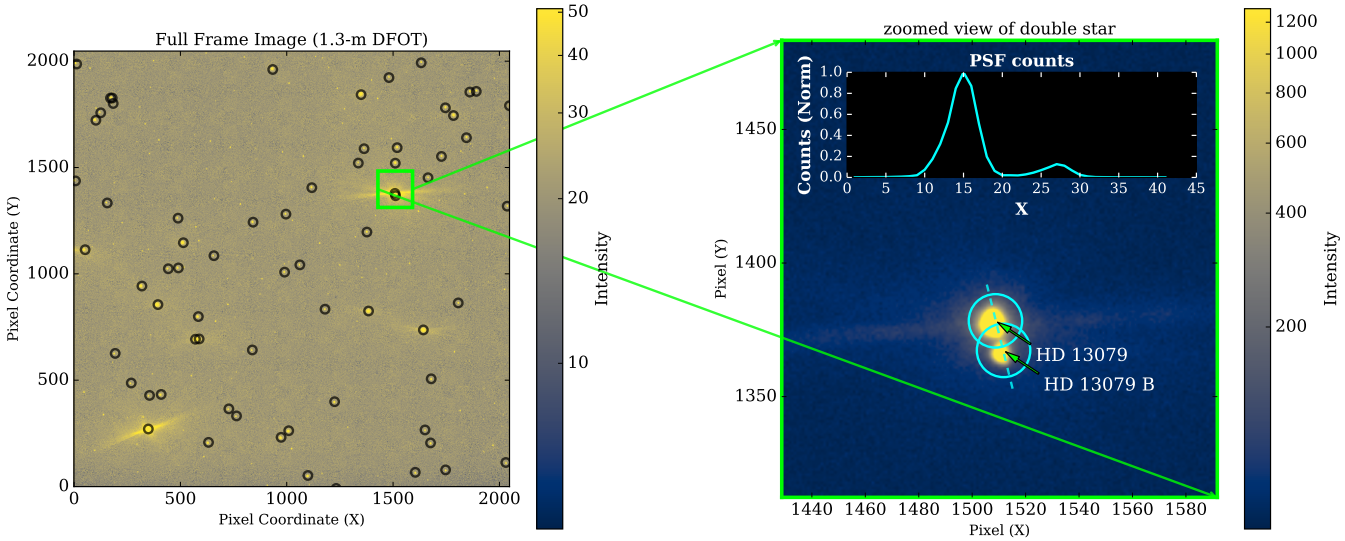

Figure 5. Left panel: The full frame image of HD 13079 and its companion HD 13079B observed with the 1.3-m DFOT. The objects shown in the black circles are stars present on the field, which are used as comparison stars to remove the common trend and employ the differential photometry. Right panel: The zoomed-in version of the double star that is clearly resolved from the ground-based photometry. The dotted line intersecting the two stars represents the point spread function (PSF). The double Gaussian depicted in the inset illustrates the pixel counts along the line in the zoomed image corresponding to an angular separation of 6.48 ± 2.70 *arcsec*.

2023). This temperature aligns with the effective temperatures expected for solar-like oscillators. Consequently, pulsation frequencies can be expected due to the contaminated flux in the region of solar-like oscillations. To differentiate the fluxes originating from HD 13079B, we performed the differential photometry using ground-based observations that possess better spatial resolution compared to the *TESS* pixels.

3.2 Ground-based Photometry

The ground-based photometric observations of HD 13079 and its companion, HD 13079B were conducted using the 1.3-m Devasthal Fast Optical Telescope (DFOT) located at Devasthal and operated by the Aryabhatta Research Institute of Observational Sciences (ARIES). This telescope features a plate of scale 0.54 *arcsec* pixel^{-1} and is equipped with a CCD array of 2048×2048 pixels together with high-efficiency transmission filters yielding a field of view (FoV) of 18′ × 18′ (Joshi et al. 2022a). The left panel of Fig. 5 illustrates the FoV of the CCD containing HD 13079 and other field stars, while the

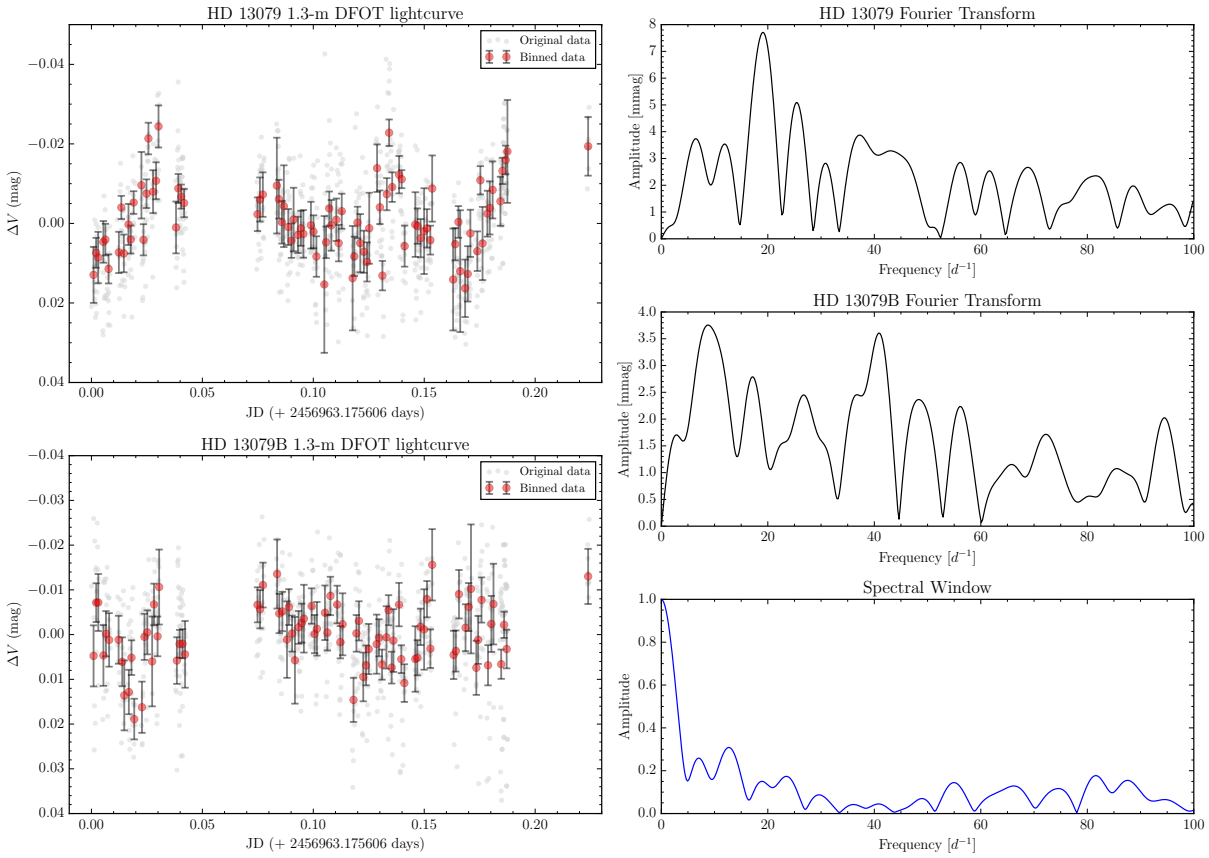

Figure 6. Left Panels: The original light curves of HD 13079 and HD 13079B acquired from the 1.3-m DFOT are shown with grey scatter points while the binned (10 points) time-series data is represented with red error bars. Right panels: The upper and middle panels display the matched frequency spectra, while the lower panel illustrates the spectral window for the combined time-series string.

right panel shows a zoomed-in view of the double star HD 13079 and HD 13079B (bottom part) together with the PSF profile (top part).

The time-series photometric observations were obtained through the Johnson V-band on November 1, 2014. A total of 792 science frames were acquired, each having an exposure duration of 5 seconds. Standard data reduction procedures involving bias subtraction, flat-field correction and cosmic ray removal were implemented utilising the IRAF package (Tody 1986). The PSF photometry was subsequently utilised with the DAOPHOTII package (Stetson 1992) to extract the light curves of all stars presented in the field. The angular separation between HD 13079 and HD 13079B ascertained from the PSF peak positions was calculated to be 6.48 ± 2.70 *arcsec*.

To eliminate long-term light variations, systematic trends to all light curves were identified and subsequently removed from the time-series data of HD 13079 and HD 13079B. The resultant light curves are depicted in the left panel of Fig. 6 while the corresponding frequency spectra are illustrated in the right panel of the same figure. The extracted frequencies along with their amplitudes and phases are tabulated in Table A1. Nonetheless, due to its temperature comparable to that of the Sun, the secondary star HD 13079B is expected to have solar-type oscillations and generally the intrinsic oscillations peaks found in the high-frequency domain ($> 86\ d^{-1}$) (Balona 2020) and is unlikely to overlap with the HD 13079 spectra. The frequency spectra of HD 13079B shown in Fig. 6 indicate weak signals in the frequency range below $50\ d^{-1}$. However, no radial modes are identified in the *TESS* light curve of HD 13079 within the frequency resolution (i.e., $\pm 6\ d^{-1}$) of the two most dominant modes $< 50\ d^{-1}$ observed in the spectra of HD 13079B. Therefore, the identification and removal of the contaminations are crucial for modelling and analysing the multi-periodic photometric variability observed in the targets.

4 MODE IDENTIFICATION

The pulsations in δ Sct stars are generally classified as low-order radial and/or non-radial modes (Breger 2009). For higher angular degrees ($\ell \geq 4$), the pulsation amplitudes decrease due to cancellation effects throughout the star disc (Aerts et al. 2010). Nonetheless, some of the δ Sct stars exhibit complex frequency spectra, making it difficult to identify the pulsation modes. The following subsections provide the identification of the pulsation modes using several methods, namely, échelle diagrams, Q-values and frequency ratios.

4.1 Échelle Diagram

An échelle diagram is a graphical representation to illustrate the regularities in frequency spectra. The frequency spectra of intermediate mass stars have a pattern of regular vertical ridges that are evident in the high-frequency regime, which are associated with pure p-modes; conversely, in the low-frequency regime, the visible curved ridges may result from the coupling of g-modes (Bedding et al. 2020). However, in some of the cases, the échelle diagrams do not clearly

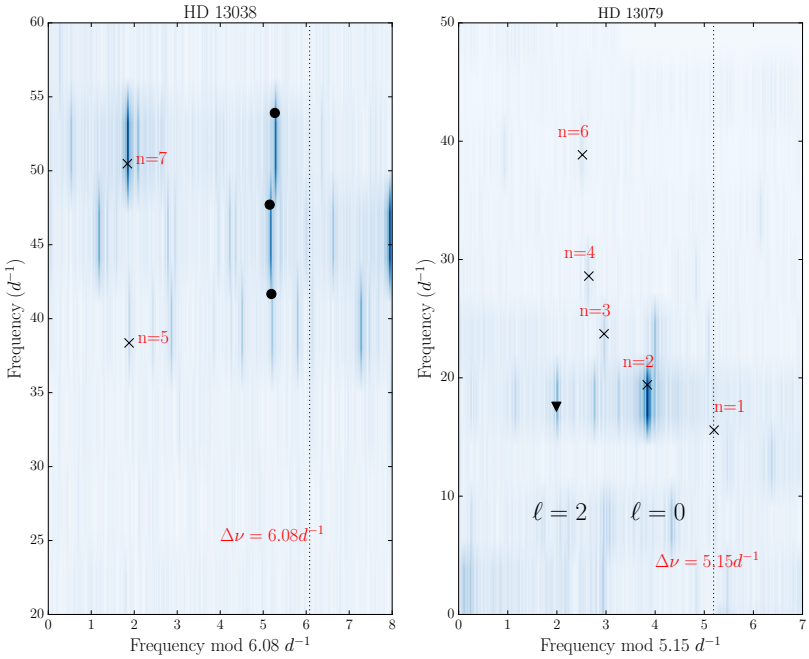

Figure 7. The left panel shows the échelle diagram of HD 13038 constructed from the combined *TESS* time-series data, where frequencies marked with crosses and filled circles correspond to the left and right ridges, respectively. The right panel presents the same for HD 13079, in which the crosses indicate the identified radial modes and the triangle marks the quadrupole mode.

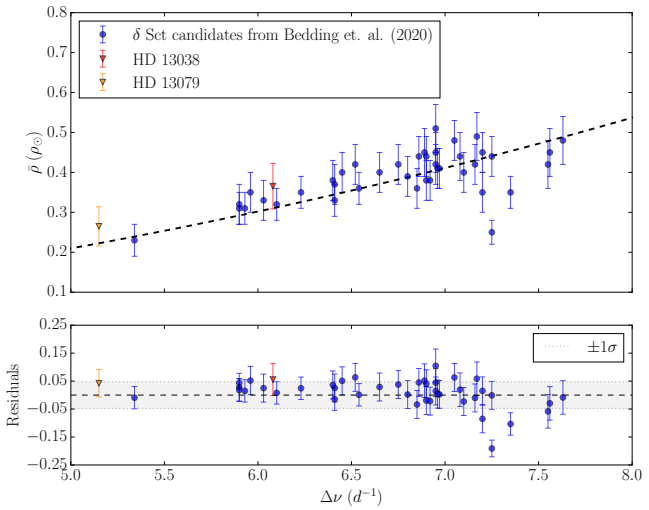

Figure 8. Comparison of large frequency separation ($\Delta\nu$) and mean stellar density ($\bar{\rho}/\rho_\odot$) relation for HD 13038 and HD 13079 with the δ Sct samples taken from Bedding et al. (2020).

visualise vertical ridge patterns associated with regularly spaced radial modes. The high order p-modes ($n \gg \ell$) exhibit regular spacing and approximately adhere to the asymptotic relation (Vandakurov 1967; Tassoul 1980) expressed as:

$$\nu_{n,\ell} = \Delta\nu \left(n + \frac{\ell}{2} + \epsilon \right), \tag{1}$$

where $\Delta\nu$ is the large frequency separation and ϵ represents a phase term of the order unity, n indicates radial order and l signifies angular degree. The inverse of the large frequency separation ($\Delta\nu$) corresponds to the acoustic travel time across the stellar diameter. The parameter $\Delta\nu$ essentially grows with the square root of the mean stellar density ($\bar{\rho}$) (Vandakurov 1967) and can be estimated observationally by adjusting the dynamic échelle diagram interface until the ridges align (Hey & Ball 2022).

The échelle diagrams are constructed using calibrated large frequency separations of $\Delta\nu$ = 6.08 d^{-1} and 5.15 d^{-1} for HD 13038 and HD 13079, and are shown in the left and right panels of Fig. 7, respectively. For HD 13038, two ridges (left and right), indicated by crosses and filled circles, are clearly visible. In contrast, HD 13079 shows a single prominent ridge marked by crosses, and a quintuplet structure is apparent around the frequency marked with a triangle.

Recently, Bedding et al. (2020) and Hasanzadeh et al. (2021) proposed kind of empirical relations defined as $\Delta\nu \propto 0.86\,\bar{\rho}^{0.46}$ and $\Delta\nu \propto 0.76\,\bar{\rho}^{0.46}$, respectively. To compare these relations, mean stellar densities were calculated using the formula given in Eq. 4. For this, the mass M and radius R are determined by conventional equations and the values are listed in Table 2. Fig. 8 depicts the correlation between $\Delta\nu$ and $\bar{\rho}$ where the samples for comparison were taken from Bedding et al. (2020) and found that both the quantities are strongly correlated within $1-\sigma$ uncertainty.

4.2 Frequency Ratios

For the analysis of frequency ratio, we computed the ratios of radial mode frequency to the frequency of subsequent higher-order modes. This technique was first introduced by Petersen (1973) who measured the ratios of shorter to longer periods and is now being extensively used for identifying radial orders in δ Sct pulsations (Poretti & Beltrame 2004; Balona 2016b; Furgoni 2016; Yang et al. 2021; Jia et al. 2025). In this study, we computed the radial mode frequencies for various masses with a constant overshooting parameter α_{ov} = 0.1 and hydrogen fraction $X_C < 0.745$ and two different metallicities, Z = 0.020 for HD 13038 and Z = 0.026 for HD 13079.

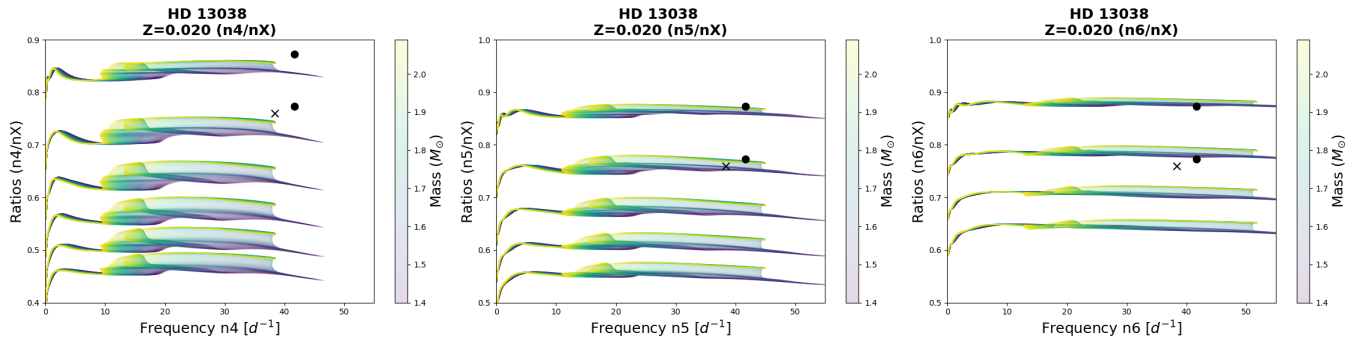

Figure 9. Frequency ratio diagrams (solid lines) calculated for HD 13038 with different masses (color coded) values in the range (1.40, 2.09) with metallicity $Z = 0.020$, $\alpha_{ov} = 0.1$ and $X_C < 0.745$. The different groups of lines correspond to increasing values of nX in the denominator from top to bottom, starting from $nX = 5$ (left), 6 (middle), and 7 (right). The observed frequency ratios for the left ridge is marked in crosses and for the right ridge in filled circles denoted in the same symbol as in the échelle diagram (left panel of Fig. 7).

The left panel of Fig. 7 displays the échelle spectra of HD 13038, which exhibit two vertical ridges. We have computed the ratios of the lowest to the highest frequencies for each ridge. For the left ridge, we identified two frequencies at 38.34 d^{-1} and 50.48 d^{-1} with a matching frequency ratio ≈ 0.760 and represented by crosses in Fig. 9. Correspondingly, for the right ridge, there are three frequencies identified as 41.67 d^{-1}, 47.71 d^{-1} and 53.90 d^{-1}. The ratio of the lowest frequency to the higher frequencies is ≈ 0.873 and 0.773, as depicted by filled circles in Fig 9. The computed ratios align with the theoretical lines for $n = 5$, representing the lowest frequency for both left and right ridges (Fig 9, middle panel). The comparison of frequency ratio diagrams for solar metallicity ($Z = 0.014$) instead of $Z = 0.020$ is shown in Fig. A2, leading to the same conclusions.

The associated frequencies in the échelle diagram of HD 13079 (Fig. 7, right panel) are 15.18 d^{-1}, 19.48 d^{-1}, 23.72 d^{-1}, 28.60 d^{-1} and 38.85 d^{-1}. The frequency ratios of the lowest to the higher frequencies are $\approx$ 0.779, 0.639, 0.530 and 0.390 and depicted in crosses in Fig. 10. The visual match between the calculated ratios and the theoretical values suggests that the lowest detected frequency in the HD 13079 spectra could either be $n = 1$ corresponding to models of $\sim 2M_\odot$ or $n = 2$ for $\sim 1.5M_\odot$. The comparison of frequency ratio diagrams for solar metallicity ($Z = 0.014$) instead of $Z = 0.026$ is shown in Fig. A3, confirming these results.

4.3 Pulsation constant

For the δ Sct stars pulsating in low-order p-modes, the pulsation constant (Q) plays an important role in identifying the radial order of pulsation modes (Breger 1990, 2000). It is defined as

$$Q = P\sqrt{\bar{\rho}/\rho_\odot}, \tag{2}$$

where P denotes the pulsation period (in days) and $\bar{\rho}$ represents the mean stellar density. Due to the applied mass range in the model grid, the Q-value of the fundamental radial mode ($n = 1$) exhibits a variation of $\delta Q/Q \approx 0.63$, diminishing with increasing radial order to $\delta Q/Q \approx 0.17$ for $n = 8$ as illustrated in Fig. 11. Some of the studies demonstrated that typical Q-values for low radial modes in δ Sct stars vary from $\sim$ 0.03 to 0.05 days, contingent upon the radial order (Fitch 1981; Suárez et al. 2005). The Q-values are calculated for various radial overtones ($n \sim$ 1–9) across different masses with $Z = 0.020$ and $Z = 0.026$ for a constant overshoot of $\alpha_{ov} = 0.1$ and illustrated in left and right panels of Fig. 11 for HD 13038 and HD 13079 respectively. A comparison of Q-values with the solar metallicity is presented in Fig. A4. The Q-value follows a relationship with metallicity, as previously indicated (Sarkar et al. 2024b); where high metallicity (Z) increases the opacity (Bate 2014), resulting in evolutionary trajectories that are characterised by reduced brightness and effective temperature. As the pulsation constant escalates with diminishing temperature (Dornan & Lovekin 2022), the reduced brightness leads to a decrease of the stellar radius (R) and narrow the mean density ($\bar{\rho}$) producing an larger Q-value as the Q value is directly proportional to the density ($Q \propto \sqrt{\bar{\rho}}$).

To calculate the Q-value for the identified radial modes, masses and mean densities were taken from Table 2). Fig. 11 shows the variation of Q with frequency associated with different radial overtones. For HD 13038, Q-values are computed for the frequencies corresponding to the right and left ridge, indicated with circles and crosses in the left panel of Fig. 7, respectively. Consequently, they are depicted by circles and crosses with error bars in Fig. 11. The prior examination of frequency ratios indicates the potential for left-ridge frequencies corresponding to radial orders $n = 5, 7$ and $n = 5, 6, 7$ for the right ridge. In the left panel of Fig. 11, the Q-values are consistent with the radial ordering for both ridges. The frequencies associated with the left and right ridges, interpreted as radial overtones, are used to derive the fundamental parameters. The seismic age is found to be consistent with the left-ridge frequencies identified as radial modes of orders $n = 5, 7$.

The Q-values computed for the frequencies of the ridges in the échelle diagram of HD 13079 (right panel of Fig. 7 as indicated by crosses) are presented by crosses with errorbars in the right panel of Fig. 11. They concur with the radial order of n=1,2,3,4 and 6, which is compatible with the left panel of the frequency ratio diagrams shown in Fig. 10.

5 ASTEROSEISMIC MODELLING

Stellar evolutionary models were generated using the code CLÉS (Scuflaire et al. 2008a) that employs OPAL 96 radiative opacity tables (Iglesias & Rogers 1996) taken from Alexander & Ferguson (1994). For the dense regions, it also incorporated conductive opacities from Itoh et al. (1994). Microscopic diffusion of hydrogen (H), helium (He) and heavy elements is analysed using the multi-component Burgers formalism (Thoul et al. 1994), incorporating resistance coefficients from Paquette et al. (1986). Radiative levitation is not accounted for in the grid used for the present investigation. The opacity tables

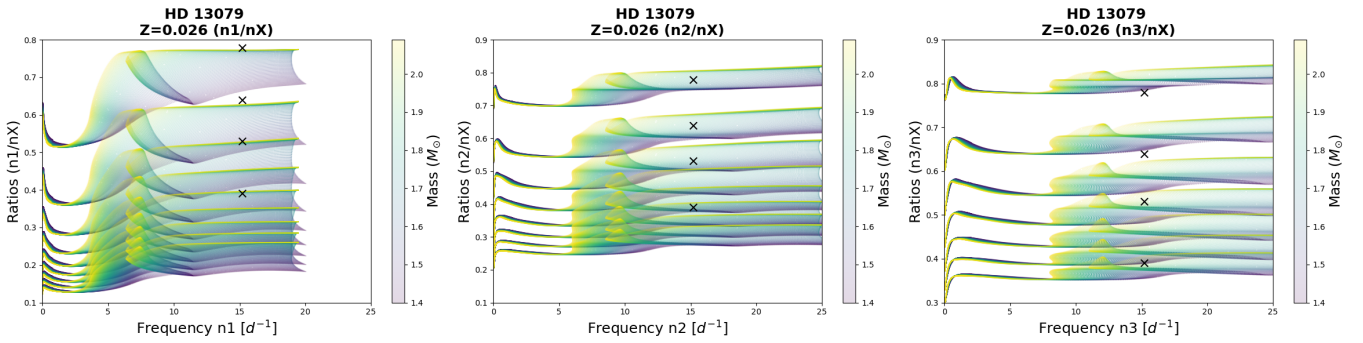

Figure 10. Frequency ratio diagrams (solid lines) calculated for HD 13079 with different masses (color coded) values in the range (1.40, 2.09) with metallicity $Z = 0.026$, $\alpha_{ov} = 0.1$ and $X_C < 0.745$. The different groups of lines correspond to increasing values of nX in the denominator from top to bottom, starting from $nX = 2$ (left), 3 (middle), and 4 (right). The crosses are corresponding to the frequency ratios calculated for *TESS* frequencies of HD 13079, marked as crosses in the échelle diagram (right panel of Fig. 7).

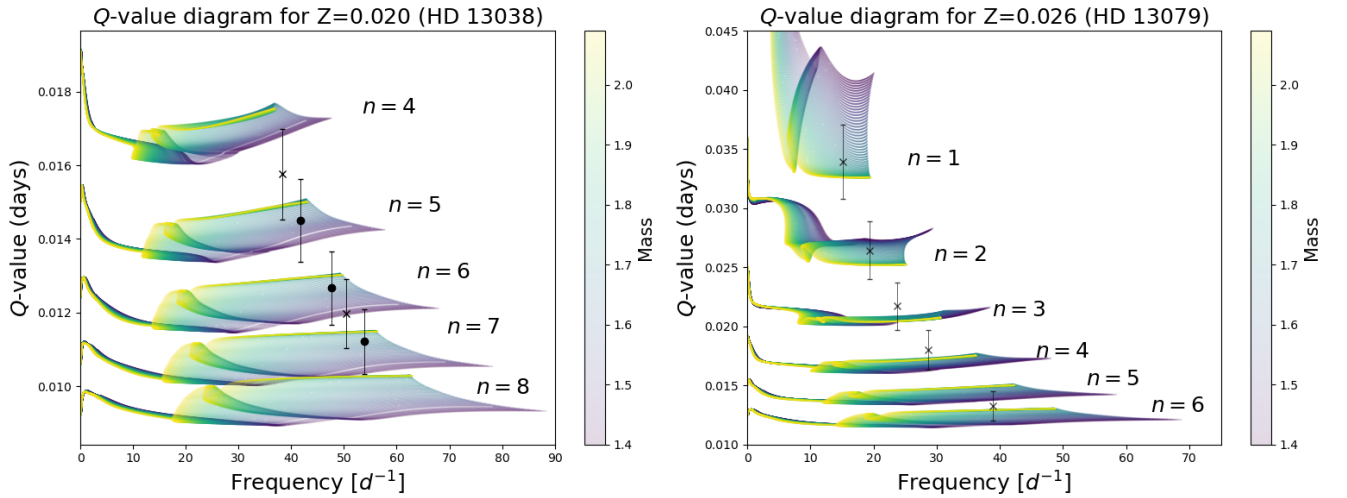

Figure 11. Left: Theoretical pulsation constants (Q-values) computed for models with $Z = 0.020$ and $X_C < 0.745$, color coded for different masses, shown for radial orders $n = 4$–8. The identified radial modes for HD 13038 are indicated by crosses and circles with error bars, corresponding to the frequencies marked with crosses and circles in the échelle diagram in Fig. 7. Right: Theoretical pulsation constants (Q-values) computed for models with $Z = 0.026$ and $X_C < 0.745$, shown for radial orders $n = 1$–6, with the identified radial modes for HD 13079 plotted in crosses with error bars.

are interpolated in $(\log T, \log R)$ domain where $R = \rho/(T/10^6\,\mathrm{K})^3$, facilitating a seamless transition across all temperature ranges.

Adiabatic radial pulsation frequencies at each evolutionary phase were computed utilising the code OSC (Scuflaire et al. 2008b). For the seismic modelling, we created dense grids of evolutionary tracks with masses ranging from 1.40 to 2.09 $M_\odot$ using an increment of 0.01 $M_\odot$.

Neither of the targets is a member of an open star cluster, nor is their global metallicity documented in the literature. Hence, within the grid, we adopted a metallicity range of $Z = 0.002 - 0.030$ in steps of 0.002. Despite the evolution of surface abundances beyond the MS, models and measurements suggest that stars younger than around 2 Gyr generally retain [Fe/H] values near or slightly deviating from the solar value (Dotter et al. 2017). For each model, we evolved the stars from a central hydrogen abundance of $X_C = 0.745$ ($\approx$ 99% of the initial hydrogen content), corresponds to the age ranging 20 − 35 Myrs, for $Z = 0.002 - 0.030$ respectively (illustrated in Fig. A5) and computed the adiabatic radial oscillation frequencies ($\ell = 0$) for overtones in the range $n = 1$ to 10.

Overshooting parameter is employed in CLÉS (Gabriel et al. 2014) at a step extension of 0.1 H_P beyond the Schwarzschild boundary (Umezu 1995; Claret & Torres 2016, 2017, 2018, 2019; Deheuvels et al. 2016). A solar composition from Asplund et al. (2009) was uniformly employed for the equation of state, opacities, and nuclear reaction rates. Outer boundary conditions were established utilising a grey Eddington atmosphere at an optical depth of $\tau = 2/3$ (Eddington 1926; Kippenhahn & Weigert 1990). Convection was treated based on the standard mixing-length theory with $\alpha_{MLT} = 1.9$, and overshooting was incorporated by permitting mixing beyond the convective boundary with mixing efficiency diminishing exponentially with distance as delineated by Herwig (2000). The thermodynamic values were obtained with FreeEOS tool (Irwin 2012).

For the seismic analysis, the identified radial modes were used to constrain the models using a seismic χ^2 minimization technique as follows (Murphy et al. 2021) :

$$\chi^2 = \sum_i^N \left(\frac{f_{c,i} - f_{o,i}}{\sigma_f} \right)^2 \quad (3)$$

where $f_{o,i}$ and $f_{c,i}$ are the observed and calculated frequencies,

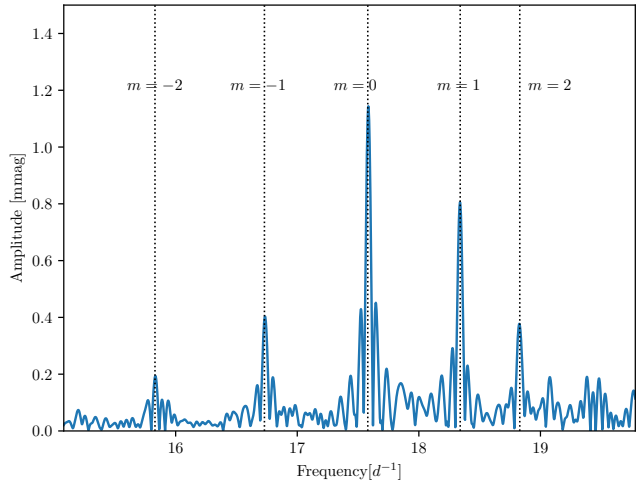

Figure 12. The rotational splitting of 17.58 d^{-1} for non-radial mode $\ell = 2$. The first radial overtone frequency at 19.41 d^{-1} is pre-whitened for clear depiction. The quintuplet peaks correspond to $m = -2, -1, 0, +1$ and $+2$ respectively.

respectively and $\sigma_f = 0.1\,d^{-1}$ is the adopted uncertainty in the frequency.

The models corresponding to the minimum χ^2 value were selected from each combination of (M, Z) and plotted them in the plane of mean stellar density ($\bar{\rho} \approx M/R^3$) against the stellar parameters (mass, radius, metallicity, age, and core H-abundance). These models are represented as black scatter points in Fig. A1. Furthermore, models situated within $1-\sigma$ range of location in the H-R diagram with the details provided in Table 1 are denoted with the red scatters in Fig. A1, which are utilised for the estimation of the seismic parameters.

6 MEAN STELLAR DENSITY

The large frequency separation ($\Delta\nu$) follows variation with the mean stellar density ($\bar{\rho}$) approximately expressed as (Bedding et al. 2020; Hasanzadeh et al. 2021),

$$\Delta\nu \propto \sqrt{\bar{\rho}} \approx \sqrt{\frac{M}{\frac{4}{3}\pi R^3}} \tag{4}$$

where M and R are the stellar mass and radius, respectively and are sourced from Table 2 for computation. Our method uses the identified radial mode frequencies as seismic constraints on the stellar models characterized by the large frequency separation $\Delta\nu \approx \nu_{n,0} - \nu_{n-1,0}$ which constrains the mean stellar density. For HD 13038, the resulting model distributions yield relative mean density uncertainties of $\delta\rho/\bar{\rho} \approx 0.049$ (Fig. A1) for the right ridge and $\delta\rho/\bar{\rho} \approx 0.057$ (Fig. A7) for the left ridge. For HD 13079, we obtain $\delta\rho/\bar{\rho} \approx 0.045$ (Fig. A8).

The models within the $1-\sigma$ range of the H-R diagram apply additional constraints on the mean stellar density. For HD 13038, it is $\delta\rho/\bar{\rho} \approx 0.002$ for the right ridge and $\delta\rho/\bar{\rho} \approx 0.0055$ corresponding to the left ridge. In the left panel of Fig. A6, we have compared the χ^2 vs mean density ($\bar{\rho}/\rho_\odot$) distributions for left and right ridges of HD 13038, both illustrating mean density within limit of the calculated value from $\log L/L_\odot$ and $\log T_{\rm eff}$ is compared in Table 2. Nevertheless, the left ridge has a broader spread and in Fig. A7, it is observed that the models within the $1-\sigma$ covers the entire range of the model parameters. However, the density distribution for the right ridge depicted in Fig. A1 is observed to be more localised. For HD 13079, the mean density determined from the $1-\sigma$ limit in the H-R diagram is $\delta\rho/\bar{\rho} \approx 0.0040$. The distribution of stellar parameters with the mean stellar density are depicted in Fig. A8 while the right panel of Fig. A6 shows relationship between χ^2 vs mean density and it is found that the seismic models are situated within the calculated range.

7 STELLAR ROTATION

The equatorial rotational velocity ($v_{\rm eq}$) of a stellar body can be approximated using the equation:

$$v_{\rm eq} = 50.6\, f_{\rm rot}\, R, \tag{5}$$

where R denotes the radius in solar units obtained from seismic density modelling and from the Stefan–Boltzmann law. Here, we have selected the mean of the two mentioned values for the calculation. Other than the spectroscopic means, rotation frequency ($f_{\rm rot}$) can be derived from the frequency spectra of time-series data. Here, for both the target stars, we have taken the $v \sin i$ from prior study by Joshi et al. (2017) as presented in Table 1 and can be used to calculate the angle of inclination (i).

7.1 HD 13038

The frequency spectra of the combined time-series data for HD 13038, as illustrated in top panel of Fig. 3, exhibit two low-frequency peaks at 0.47 d^{-1} and 0.94 d^{-1}. Upon evaluating $f_{\rm rot}$=0.47 d^{-1} as a rotation frequency and placing mean $R/R_\odot = 1.78 \pm 0.04$ into Eq. 5, yielding an equatorial velocity of $v_{\rm eq} \approx 41\,{\rm km\,s^{-1}}$ which is incompatible with the spectroscopic projected rotational velocity $v \sin i = 87 \pm 5\,{\rm km\,s^{-1}}$ presented in Table 1. Considering, $f_{\rm rot}$=0.94 d^{-1} as a rotation frequency, the equatorial velocity is approximately $v_{\rm eq} = 85 \pm 2\,{\rm km\,s^{-1}}$ which closely aligns with the reported projected rotational velocity for $i \approx 90°$. Thus, the frequency of 0.94 d^{-1} can be interpreted as the rotational frequency of HD 13038.

The frequency at 0.47 d^{-1} may be attributed to the effect of surface differential rotation. As discussed in Reinhold et al. (2013), the latitudinal differential rotation on the stellar surface causes shear on the surface, that may cause a secondary peak to appear near the rotation frequency. The study reveals that for stars with $T_{\rm eff} > 7000$ K, the horizontal shear can be $\Delta\Omega \gtrsim 1$ for fast to moderate rotators. HD 13038 is a hot star with an effective temperature of approximately 7960 K. Utilising the scaling relation (SR), $\Delta\Omega = 0.053\ (T_{\rm eff}/5130)^{8.6}$ (Reinhold et al. 2013), we calculate $\Delta\Omega_{SR} = 2.32 \pm 0.50$ rad d^{-1}. Here, considering the rotation frequency at 0.94 d^{-1} and surface differential rotation at 0.47 d^{-1}, we have calculated, $\Delta\Omega_{Obs} = 2\pi|f_1 - f_2| \approx 2.95$ rad d^{-1}. However, it has been shown that for $T_{\rm eff} > 7000$ K, the uncertainty of the points increases and becomes more scattered (Reinhold et al. 2013; Reinhold & Gizon 2015).

7.2 HD 13079

In the frequency spectra of the combined time-series observation (Table A5) of HD 13079, we have detected $f_{\rm rot}(\sim f_{30}) \sim 0.86\ d^{-1}$. The equatorial rotational velocity can be computed using Eq. 5 as $v_{\rm eq} = 84 \pm 1$ km s^{-1} where $R/R_\odot = 1.935 \pm 0.023$ is adopted as

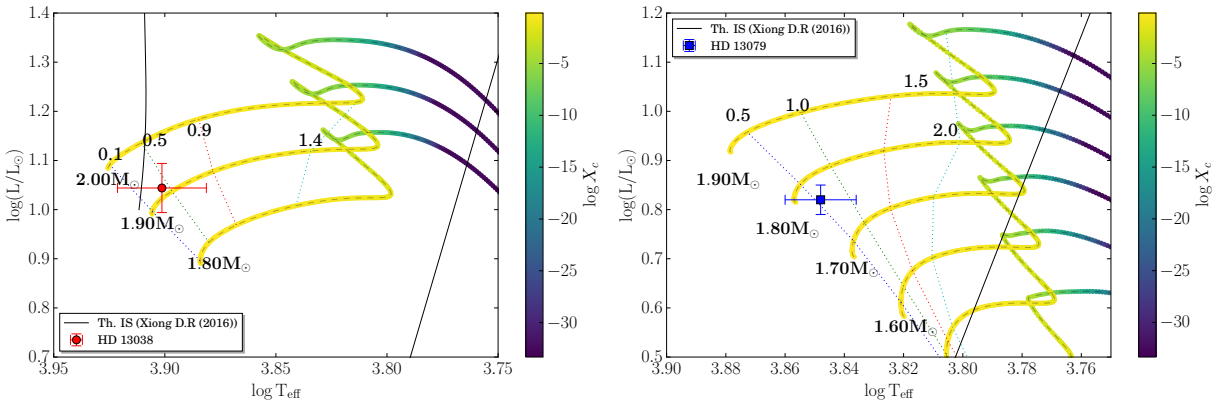

Figure 13. Evolutionary tracks calculated for $X_C < 0.745$ with $\alpha_{ov} = 0.1$ with different metallicities $Z = 0.020$ for HD 13038 (left) and $Z = 0.026$ for HD 13079 (right). The solid black line corresponds to the theoretical δ Sct instability strip calculated for low-order pressure modes (Xiong et al. 2016). The dotted lines are the isochrones computed for the evolution tracks of the different metallicity.

mean radius derived from the mean density model. The equatorial rotational velocity along with the projected rotational velocity of $v \sin i = 56 \pm 4$ km s^{-1} taken from Table 1 combined with the preceding information capitulate an inclination angle of $i = 42 \pm 4°$.

The frequency spectrum of the *TESS* time-series data for HD 13079, shown in the bottom panel of Fig. 3, exhibits rotationally induced splitting associated at 17.58 d^{-1}. The five components of the quintuplet, with azimuthal orders $m = -2$ to 2 as displayed in Fig. 12, together with the identified radial orders, indicate that this splitting corresponds to a quadrupole mode ($\ell = 2$) with radial order $n = 1$. Using the first-order rotational splitting relation, we obtain $C_{n,\ell} \simeq 0.10$, which is consistent with the expected value for quadrupole modes in δ Sct stars, as reported by Guo et al. (2024). The mean observed splitting corresponds to $f_{rot} \approx 0.77$ d^{-1}, supporting a rotation frequency of ≈ 0.86 d^{-1}, which is also detected in the frequency spectrum of the combined light curve (see Table A5).

In HD 13079, we have detected only radial ($\ell = 0$) and quadrupole ($\ell = 2$) mode frequencies. The absence of $\ell = 1$ modes has been observed in other δ Sct stars, for example, KIC 9700322 (Breger et al. 2011) where geometric cancellation and intrinsic amplitude modulation presumably diminish the visibility of dipole pulsations.
It is noteworthy, that we have also detected a dominant frequency at ≈ 0.25 d^{-1}. We excluded this value as a candidate for the rotation frequency because it falls below the range necessary for a valid solution of the inclination angle. Additionally, the observed quintuplet shows a mean splitting of 0.77 d^{-1}, suggesting that the stellar rotation frequency should be near this value to achieve a physically reasonable Ledoux constant $C_{n,\ell}$ (Guo et al. 2024).

8 EVOLUTIONARY STATUS ANALYSIS

The δ Sct stars are found near the lower MS to the subgiant region of the H-R diagram. In Sec. 5, we explored the constraints of radial mode and stellar mean density applied to the stellar models. These provide the stellar models to align almost parallel to the ZAMS and should coincide with the observed position of the star (Sarkar et al. 2024b). Here, different combinations of radial orders have been employed to constrain the models in the H-R diagram and illustrated in Fig. A9 for HD 13038 and Fig. A10 for HD 13079. The top panels of Fig. A9 depict the positions of the stellar models where the right-ridge frequencies (from the left panel of Fig.7) are employed to restrict models with various radial order combinations, whereas the bottom panels of Fig. A9 illustrate a similar approach for left-ridge frequencies.

Fig. 13 displays the H-R diagrams for $X_C < 0.745$ (i.e. $\log X_C \lesssim -0.127$) at two distinct metallicities $Z = 0.020$ and $Z = 0.026$ which corresponds to their model parameters for HD 13038 and HD 13079 respectively. The target stars are identified as being in the early-MS phase, as illustrated in the left panel of Fig. 13. The isochrones indicated by the dotted lines suggest that the mass and age of HD 13038 are within $1.85 - 1.95 M_\odot$ and approximately 0.1 Gyr to 0.8 Gyr, respectively. Similarly, for HD 13079 the position depicted in the right panel of Fig. 13, the mass and age lie in the range $1.70 - 1.80 M_\odot$ and 0.1 – 1.0 Gyr, respectively. The parameters estimated from the H-R diagrams agree to those computed from the mean density distribution, and are compared in Table 2.

9 RESULTS AND CONCLUSIONS

The asteroseismic investigation of the two mild Am candidates, HD 13038 and HD 13079, represents a further step toward a comprehensive understanding of the pulsational behaviour of chemically peculiar (CP) stars. In the present study, we make extensive use of multi-sector, multi-cadence, high-precision *TESS* observations, complemented by ground-based data. The precisely determined pulsation frequencies are employed to carry out asteroseismic modelling based on an extensive grid of stellar mass and metallicity. This analysis leads to the following main results and conclusions:

- HD 13038 is a hot ($T_{eff} \approx 7960$ K) mild Am δ Sct star near the blue-edge of the instability strip, with essentially negligible *TESS* pixel contamination ($\approx 4\%$). Multi-sector *TESS* photometry of HD 13038 yields 37 pulsation frequencies with SNR > 5. HD 13079 is a cooler ($T_{eff} \approx 7040$ K) mild Am δ Sct with a nearby companion (HD 13079B at 6.48 ± 2.70 *arcsec*), leading to $\approx 15\%$ flux contamination in *TESS* . Dedicated PSF photometry from 1.3-m DFOT time-series data of HD 13079/13079B identified two low-amplitude frequencies (8.74 ± 6.00 and 41.02 ± 6.00 d^{-1}) with SNR=4 in the companion and a dominant frequency 19.06 ± 6.00 d^{-1} in HD 13079. However, we found that the identified radial modes do not coincide with the detected frequency range of HD 13079B, yet they serve as essential inputs for the asteroseismic modelling.
- For HD 13038, a combined light curve was used to construct

Table 2. Seismic values of mass, metallicity, age, stellar radius, mean stellar density, core H-abundance and equatorial rotation velocity for stars HD 13038 and HD 13079 found in the current study using median values of models constrained within $1-\sigma$ error of the observed $\log L/L_\odot$ and $\log T_{\rm eff}$. The errors of the parameters correspond to the standard deviation of the models mentioned above.

Parameter	HD 13038		HD 13079	
	Measured/calculated	Seismic	Measured/calculated	Seismic
$M/M_\odot$	1.90 ± 0.05	1.900 ± 0.143	1.75 ± 0.05	1.790 ± 0.071
Z	–	0.0200 ± 0.0072	–	0.026 ± 0.005
Age (Gyr)	0.1-0.8	0.540 ± 0.269	0.1-1.0	1.139 ± 0.134
Radius ($R_\odot$)	1.765 ± 0.089	1.793 ± 0.043	1.873 ± 0.107	1.938 ± 0.023
$\bar{\rho}/\bar{\rho_\odot}$	0.3656 ± 0.0570	0.330 ± 0.002	0.265 ± 0.049	0.246 ± 0.001
X_C	–	0.6003 ± 0.0931	–	0.50 ± 0.04
$v_{\rm eq}$ (km s^{-1})	–	85 ± 2	–	81 ± 3
[Fe/H]	0.09 ± 0.19	-	-0.18 ± 0.15	

a dynamic échelle diagram with large separation $\Delta\nu \approx 6.08\ d^{-1}$. This reveals two nearly vertical ridges of frequencies. Analysis of frequency ratios and pulsation constants shows that the left-ridge modes correspond to radial overtones $n = 5$ and 7, while the right-ridge modes correspond to $n = 5, 6, 7$. For HD 13079, the combined *TESS* light curve yields $\Delta\nu \approx 5.15\ d^{-1}$ in the échelle diagram. The diagram shows one clear $\ell = 0$ (radial) ridge and a separate quadrupole mode ($\ell = 2$). There, frequency ratio and Q-value analysis identify the radial mode frequencies as orders $n = 1, 2, 3, 4, 6$ (and the quadrupole ridge has a mode at $n = 1$). These identifications of radial modes are used as constraints in the seismic modelling.

- After applying the constraint of radial modes to the seismic models, they tend to be aligned parallel to ZAMS line in the H-R diagram. For HD 13038, both the left- and right-ridge model sequences intersect the star's observed $T_{\rm eff}$ and $\log L/L_\odot$. The left-ridge models imply a mean density spread $\delta\rho/\bar{\rho} \approx 0.59\%$, and the right-ridge models by $\approx 0.26\%$. For both the ridges the seismic mean density lies within the calculated range. For HD 13079, models incorporating the identified radial modes also overlap with observed location in H-R diagram, with a mean-density spread $\approx 0.4\%$. In each case the seismic mean densities agree with the densities computed from independent luminosity/radius estimates, showing consistency of the models.

The two ridge solutions lead to distinct age estimates for HD 13038. For the right-ridge, the corresponding mean-density distribution shows model solutions at very early evolutionary stages (from ~ 40 Myr onwards), and the 1σ constraint in the H–R diagram yields a young age of $\approx 0.253 \pm 0.125$ Gyr, placing the star near the zero-age main sequence or in the pre-main-sequence phase. In contrast, the left-ridge solution appears from ~ 250 Myr onwards, and models within the 1σ region in this case indicate an age of $\approx 0.540 \pm 0.269$ Gyr, which is compatible with a more evolved main-sequence star. As HD 13038 is an Am star whose chemical peculiarities are expected to arise from radiative diffusion in a stable, predominantly radiative envelope conditions not typical of very young pre-MS stars. We therefore adopt the left-ridge solution as radial modes of orders $n = 5$ and 7. Furthermore, the frequencies found in the right-ridge might represent non-radial modes, which require further investigation to verify.. For HD 13079, the seismic modelling yields an age of $\approx 1.139 \pm 0.134$ Gyr (with $X_C \approx 0.50$), confirming that it is a MS star.

- The fundamental stellar parameters are estimated from the median of the mean density distribution. HD 13038 (left-ridge solution) has $M \approx 1.900 \pm 0.143\ M_\odot$ and $Z \approx 0.020 \pm 0.007$. HD 13079 has $M \approx 1.790 \pm 0.071\ M_\odot$ and $Z \approx 0.026 \pm 0.005$. These values are consistent with the position of the star in the H-R diagram. The inferred metallicities are slightly super-solar, whereas spectroscopic [Fe/H] is near- or sub-solar for HD 13038 and HD 13079. The primary reason behind such discrepancy is the effect of chemical peculiarity of the candidates for which the microscopic diffusion and radiative levitation can alter the surface abundances.
- The analysis of the rotation frequency indicates a potential rotation for HD 13038 at $f_{\rm rot} \approx 0.94\ d^{-1}$, corresponding to an equatorial velocity of $v_{\rm eq} \approx 85$ km s^{-1}. The combination of its $v \sin i$ yields $i \approx 90°$, suggesting a nearly equator-on orientation. A dominant frequency of $0.47\ d^{-1}$ has been detected, most likely attributed to surface differential rotation, and is consistent with the absolute shear calculated at the corresponding temperature. For HD 13079, combined time-series TESS observations suggest a potential rotation frequency of $f_{\rm rot} \approx 0.86\ d^{-1}$. This finding corresponds with the mean quintuplet splitting of approximately $0.77\ d^{-1}$, resulting in an equatorial velocity of $v_{\rm eq} \approx 81 \pm 3$ km s^{-1} and an inclination of $i \approx 42°$. Another dominant frequency is found near $\approx 0.25\ d^{-1}$ and found not suitable to be due to rotation and may be due to some other origin. Further investigations demand to confirm the rotational frequencies.

The targets of the present study, HD 13038 and HD 13079 are classified as mild Am δ Sct variables with effective temperatures of around 7960 K and 7040 K, respectively. Having their locations near the blue edge and near the centre of the δ Sct instability strips, excitation of high-order radial modes are intriguing. Therefore, the present study would be an important milestone towards understanding the excitation of high-order pulsation modes in Am δ Sct stars in the presence of physical processes responsible for the chemical peculiarity.

ACKNOWLEDGEMENTS

The work presented here is supported by the Belgo-Indian Network for Astronomy and Astrophysics (BINA), sanctioned by the Department of Science and Technology (DST, Government of India; DST/INT/Belg/P-09/2017) and the Belgian Federal Science Policy Office (BELSPO, Government of Belgium; BL/33/IN12). SJ and SCG acknowledge the financial support received from the BRICS grant DST/ICD/BRICS/Call-5/SAPTARISI/2023(G). G.B. acknowledges funding from the Fonds National de la Recherche Scientifique (FNRS) as a postdoctoral researcher. A.D. acknowledges the financial support received from the DST-INSPIRE Fellowship Programme (DST/INSPIRE Fellowship/2020/IF200245).

DATA AVAILABILITY

The time-series flux data from the *TESS* mission for the target stars are publicly available from the NASA MAST archive (https://mast.stsci.edu/portal/Mashup/Clients/Mast/Portal.html), and complementary ground-based time-series observations from the 1.3-m DFOT were obtained at the ARIES observing facility. This work has also made use of data from the European Space Agency (*ESA*) mission *Gaia* (https://www.cosmos.esa.int/gaia), processed by the Gaia Data Processing and Analysis Consortium (DPAC, https://www.cosmos.esa.int/web/gaia/dpac/consortium), with funding for DPAC provided by national institutions, in particular those participating in the Gaia Multilateral Agreement. In addition, this research has made use of the SIMBAD database, operated at CDS, Strasbourg, France.

REFERENCES

Abt H. A., 1961, ApJS, 6, 37
Abt H. A., Levy S. G., 1985, ApJS, 59, 229
Aerts C., Christensen-Dalsgaard J., Kurtz D. W., 2010, Asteroseismology. Astronomy and Astrophysics Library, Springer, Dordrecht, doi:10.1007/978-1-4020-5803-5
Alexander D. R., Ferguson J. W., 1994, ApJ, 437, 879
Aller A., Lillo-Box J., Jones D., Miranda L. F., Barceló Forteza S., 2020, A&A, 635, A128
Andrae R., et al., 2023, A&A, 674, A27
Antoci V., Cunha M., Houdek G., et al., 2019, Monthly Notices of the Royal Astronomical Society, 490, 4040
Asplund M., Grevesse N., Sauval A. J., Scott P., 2009, ARA&A, 47, 481
Balona L. A., 2016b, MNRAS, 459, 1097
Balona L. A., 2016a, Monthly Notices of the Royal Astronomical Society, 459, 1097
Balona L. A., 2020, Frontiers in Astronomy and Space Sciences, 7, 85
Baran A. S., Koen C., Pokrzywka B., 2015, MNRAS, 448, L16
Bate M. R., 2014, MNRAS, 442, 285
Bedding T. R., et al., 2020, Nature, 581, 147
Boiarchuk A. A., Savanov I. S., 1986, in Cowley C. R., Dworetsky M. M., Megessier C., eds, Astrophysics and Space Science Library Vol. 125, IAU Colloquium 90: Upper Main Sequence Stars with Anomalous Abundances. p. 433, doi:10.1007/978-94-009-4714-6_67
Breger M., 1990, Delta Scuti Star Newsletter, 2, 13
Breger M., 2000, Baltic Astronomy, 9, 149
Breger M., 2009, in Guzik J. A., Bradley P. A., eds, American Institute of Physics Conference Series Vol. 1170, Stellar Pulsation: Challenges for Theory and Observation. pp 410–414 (arXiv:0910.1446), doi:10.1063/1.3246530
Breger M., Pikall H., Pamyatnykh A. A., Garrido R., 1999, in Gimenez A., Guinan E. F., Montesinos B., eds, Astronomical Society of the Pacific Conference Series Vol. 173, Stellar Structure: Theory and Test of Connective Energy Transport. p. 345
Breger M., et al., 2011, MNRAS, 414, 1721
Chang S. W., Protopapas P., Kim D. W., Byun Y. I., 2013, AJ, 145, 132
Christensen-Dalsgaard J., 2008, Ap&SS, 316, 113
Claret A., 2004, A&A, 424, 919
Claret A., Torres G., 2016, A&A, 592, A15
Claret A., Torres G., 2017, ApJ, 849, 18
Claret A., Torres G., 2018, ApJ, 859, 100
Claret A., Torres G., 2019, ApJ, 876, 134
Deheuvels S., Brandão I., Silva Aguirre V., Ballot J., Michel E., Cunha M. S., Lebreton Y., Appourchaux T., 2016, A&A, 589, A93
Dileep A., Joshi S., Kurtz D. W., 2024, Bulletin de la Societe Royale des Sciences de Liege, 93, 227
Dileep A., et al., 2025a, MNRAS, 538, 1747
Dileep A., et al., 2025b, MNRAS, 542, 747
Dornan V., Lovekin C. C., 2022, ApJ, 924, 130
Dotter A., Conroy C., Cargile P., Asplund M., 2017, The Astrophysical Journal, 840, 99
Dürfeldt-Pedros O., Antoci V., Smalley B., Murphy S., Posilek N., Niemczura E., 2024, A&A, 690, A104
Eddington A. S., 1926, The Internal Constitution of the Stars. Cambridge University Press, Cambridge, doi:10.1017/CBO9780511600005
Fitch W. S., 1981, Pulsating Stars. Cambridge University Press
Furgoni R., 2016, The Journal of the American Association of Variable Star Observers, 44, 6
Gabriel M., Noels A., Montalbán J., Miglio A., 2014, A&A, 569, A63
Girish V., et al., 2001, A&A, 380, 142
Guo Z., Bedding T. R., Pamyatnykh A. A., Kurtz D. W., Li G., Gautam A., Murphy S. J., Aerts C., 2024, MNRAS, 535, 2927
Guzik J. A., Jackiewicz J., Hedlund A. M., 2022, Frontiers in Astronomy and Space Sciences, Volume 9 - 2022
Hall O. J., et al., 2022, in The 21st Cambridge Workshop on Cool Stars, Stellar Systems, and the Sun. Cambridge Workshop on Cool Stars, Stellar Systems, and the Sun. p. 128, doi:10.5281/zenodo.7543949
Hasanzadeh A., Safari H., Ghasemi H., 2021, MNRAS, 505, 1476
Hauck B., Mermilliod M., 1998, A&AS, 129, 431
Hauck B., North P., 1993, A&A, 269, 403
Herwig F., 2000, A&A, 360, 952
Hey D., Ball W., 2022, echelle: Dynamic echelle diagrams for asteroseismology, Astrophysics Source Code Library (ascl:2207.005), doi:10.5281/zenodo.3629933, https://ascl.net/2207.005
Iglesias C. A., Rogers F. J., 1996, ApJ, 464, 943
Iliev I. K., Budaj J., 2008, Contributions of the Astronomical Observatory Skalnate Pleso, 38, 129
Irwin A. W., 2012, Astrophysics Source Code Library, p. ascl:1211.002
Itoh N., Hayashi H., Nishikawa A., Kohyama Y., 1994, ApJ, 436, 418
Jenkins J. M., et al., 2016, in Chiozzi G., Guzman J. C., eds, Society of Photo-Optical Instrumentation Engineers (SPIE) Conference Series Vol. 9913, Software and Cyberinfrastructure for Astronomy IV. p. 99133E, doi:10.1117/12.2233418
Jia Q., Chen X., Wang S., Deng L., Zhang J., Jiang Q., 2025, ApJ, 984, 89
Joshi S., Joshi Y. C., 2015, Journal of Astrophysics and Astronomy, 36, 33
Joshi S., et al., 2003, MNRAS, 344, 431
Joshi S., Mary D. L., Martinez P., Kurtz D. W., Girish V., Seetha S., Sagar R., Ashoka B. N., 2006, A&A, 455, 303
Joshi S., Mary D. L., Chakradhari N. K., Tiwari S. K., Billaud C., 2009, A&A, 507, 1763
Joshi S., Ryabchikova T., Kochukhov O., Sachkov M., Tiwari S. K., Chakradhari N. K., Piskunov N., 2010, MNRAS, 401, 1299
Joshi S., et al., 2012, MNRAS, 424, 2002
Joshi S., et al., 2016, A&A, 590, A116
Joshi S., Semenko E., Moiseeva A., Sharma K., Joshi Y. C., Sachkov M., Singh H. P., Yerra B. K., 2017, MNRAS, 467, 633
Joshi Y. C., Bangia T., Jaiswar M. K., Pant J., Reddy K., Yadav S., 2022a, Journal of Astronomical Instrumentation, 11, 2240004
Joshi S., et al., 2022b, MNRAS, 510, 5854
Joshi S., et al., 2025, MNRAS, 543, 640
Kallinger T., et al., 2010, A&A, 509, A77
Kippenhahn R., Weigert A., 1990, Stellar Structure and Evolution. Astronomy and Astrophysics Library, Springer-Verlag, Berlin, Heidelberg, doi:10.1007/978-3-642-61523-8
Lenz P., Breger M., 2005, CoAst, 146, 53
Liakos A., Niarchos P., 2017, MNRAS, 465, 1181
Lightkurve Collaboration et al., 2018, Lightkurve: Kepler and TESS time series analysis in Python, ascl soft (ascl soft:1812.013)
Martinez-Vazquez C. E., Salinas R., Vivas A. K., Catelan M., 2023, in American Astronomical Society Meeting Abstracts #241. p. 177.10
Martinez P., Kurtz D. W., Ashoka B. N., 1998, Information Bulletin on Variable Stars, 4593, 1
Martinez P., et al., 1999a, MNRAS, 309, 871
Martinez P., Ashoka B. N., Kurtz D. W., Gupta S. K., Chaubey U. S., 1999b, Information Bulletin on Variable Stars, 4677, 1
Martinez P., et al., 2001a, A&A, 371, 1048
Martinez P., et al., 2001b, A&A, 371, 1048

Michaud G., 1970a, Astrophysical Journal, 160, 641
Michaud G., 1970b, ApJ, 160, 641
Monaghan J. J., 1970, A&A, 6, 464
Murphy S. J., 2014, PhD thesis, Univ. Central Lancashire, doi:10.1007/978-3-319-09417-5
Murphy S. J., Hey D. R., Van Reeth T., Bedding T. R., 2019, Monthly Notices of the Royal Astronomical Society, 485, 2380
Murphy S. J., Joyce M., Bedding T. R., White T. R., Kama M., 2021, MNRAS, 502, 1633
Nsamba B., et al., 2021, MNRAS, 500, 54
Panda S. K., Dhanpal S., Murphy S. J., Hanasoge S., Bedding T. R., 2024, ApJ, 960, 94
Paquette C., Pelletier C., Fontaine G., Michaud G., 1986, ApJS, 61, 177
Paxton B., et al., 2013, ApJS, 208, 4
Petersen J. O., 1973, A&A, 27, 89
Poretti E., Beltrame M., 2004, Communications in Asteroseismology, 145, 55
Preston G. W., 1974, ARA&A, 12, 257
Reese D., Lignières F., Rieutord M., 2008, A&A, 481, 449
Reinhold T., Gizon L., 2015, A&A, 583, A65
Reinhold T., Reiners A., Basri G., 2013, A&A, 560, A4
Rendle B. M., et al., 2019, MNRAS, 484, 771
Ricker G. R., et al., 2015, Journal of Astronomical Telescopes, Instruments, and Systems, 1, 014003
Saffe C., et al., 2020, A&A, 641, A145
Sarkar M., Joshi S., De Cat P., 2024a, Bulletin de la Societe Royale des Sciences de Liege, 93, 285
Sarkar M., et al., 2024b, MNRAS, 534, 3211
Savanov I. S., 1995, Azh, 72, 733
Savanov I. S., 1998, Astronomy Reports, 42, 508
Scuflaire R., Théado S., Montalbán J., Miglio A., Bourge P.-O., Godart M., Thoul A., Noels A., 2008a, Ap&SS, 316, 83
Scuflaire R., Montalbán J., Théado S., Bourge P. O., Miglio A., Godart M., Thoul A., Noels A., 2008b, Ap&SS, 316, 149
Smalley B., et al., 2017, MNRAS, 465, 2662
Stetson P. B., 1992, in Worrall D. M., Biemesderfer C., Barnes J., eds, Astronomical Society of the Pacific Conference Series Vol. 25, Astronomical Data Analysis Software and Systems I. p. 297
Suárez J. C., Bruntt H., Buzasi D., 2005, A&A, 438, 633
Suárez J. C., García Hernández A., Moya A., Rodrigo C., Solano E., Garrido R., Rodón J. R., 2014, A&A, 563, A7
Tassoul M., 1980, ApJS, 43, 469
Theodoridis A., Tayar J., 2025, in American Astronomical Society Meeting Abstracts #245. p. 353.06
Thoul A. A., Bahcall J. N., Loeb A., 1994, ApJ, 421, 828
Tody D., 1986, in Crawford D. L., ed., Society of Photo-Optical Instrumentation Engineers (SPIE) Conference Series Vol. 627, Instrumentation in astronomy VI. p. 733, doi:10.1117/12.968154
Twicken J. D., Chandrasekaran H., Jenkins J. M., Gunter J. P., Girouard F., Klaus T. C., 2010, in Radziwill N. M., Bridger A., eds, Society of Photo-Optical Instrumentation Engineers (SPIE) Conference Series Vol. 7740, Software and Cyberinfrastructure for Astronomy. p. 77401U, doi:10.1117/12.856798
Umezu M., 1995, MNRAS, 276, 1287
Van Reeth T., Tkachenko A., Aerts C., 2016, A&A, 593, A120
Vandakurov Y. V., 1967, Azh, 44, 786
Wang Y., Li T., Bi S., Bedding T. R., Li Y., 2023, ApJ, 953, 182
Xiong D. R., Deng L., Zhang C., Wang K., 2016, MNRAS, 457, 3163
Xu Y., Li Z.-P., Deng L.-C., Xiong D.-R., 2002, Chinese J. Astron. Astrophys., 2, 441
Yang T.-Z., Zuo Z.-Y., Wang X.-Y., Sun X.-Y., Tang R.-X., 2021, arXiv e-prints, p. arXiv:2110.13594

APPENDIX A: SOME EXTRA MATERIAL

This paper has been typeset from a TEX/LATEX file prepared by the author.

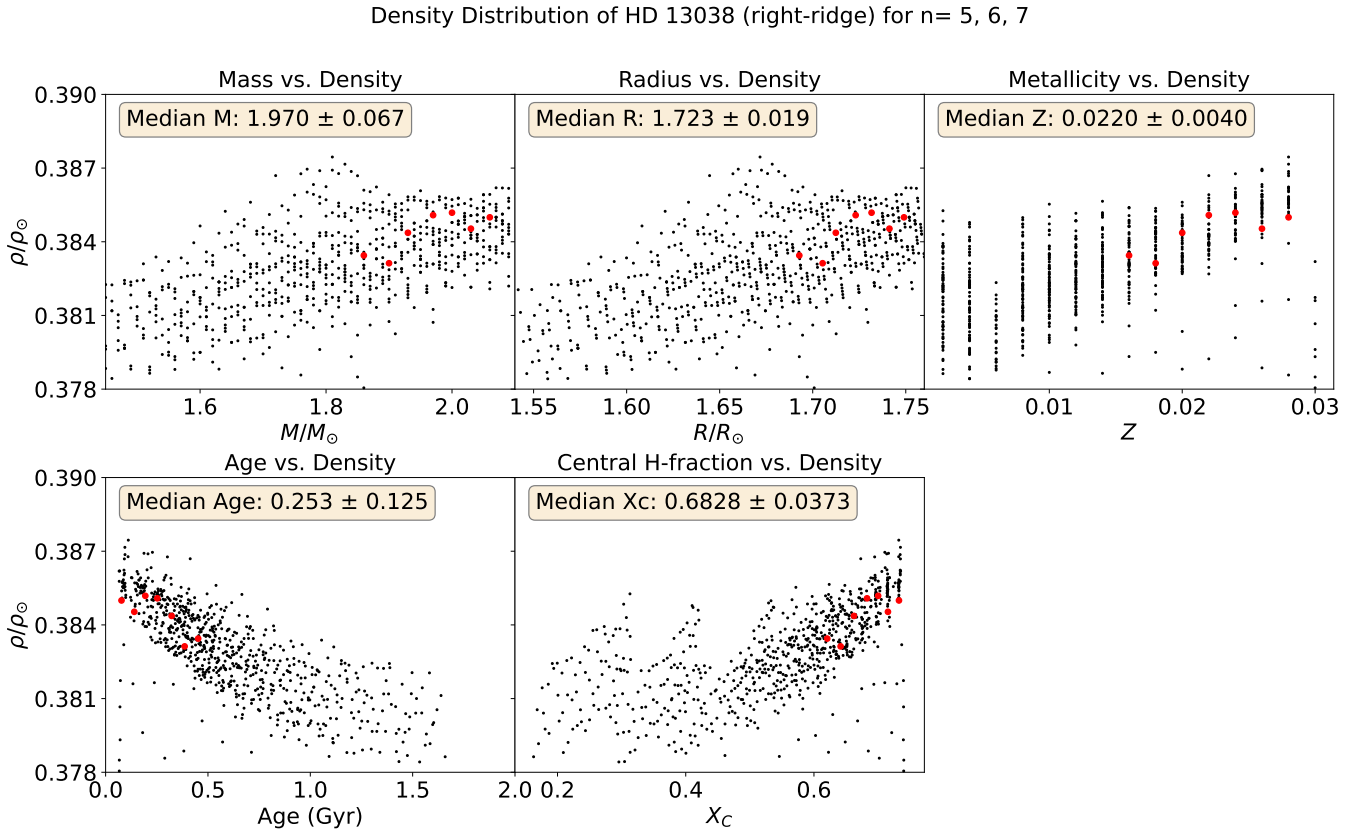

Figure A1. The plot shows the distribution of mean stellar density vs mass, radius, metallicity, age, X_C for the star HD 13038 corresponding to the right ridge with $n = 5, 6$ and 7. The black scatters correspond to the stellar model satisfying the least-χ^2 value of each (M, Z) grid, and red points are the points corresponding to the stellar models among them that are located in the $1-\sigma$ position in the H-R diagram, the median of which are considered as the best-fit parameters.

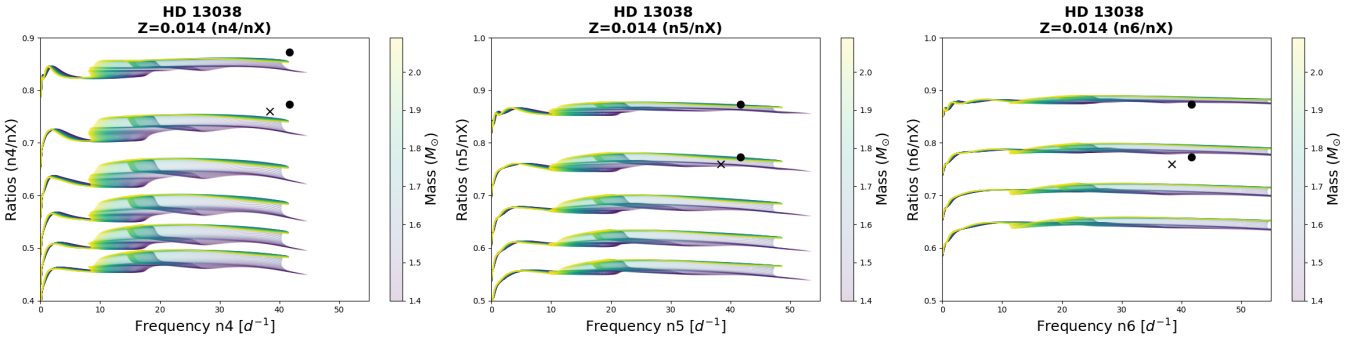

Figure A2. Frequency ratio diagrams (solid lines) calculated for HD 13038 with different masses (color coded) values in the range (1.40, 2.09) with solar metallicity $Z = 0.014$, $\alpha_{ov} = 0.1$ and $X_C < 0.745$. The different groups of lines correspond to increasing values of nX in the denominator from top to bottom, starting from $nX = 5$ (left), 6 (middle), and 7 (right). The observed frequency ratios for the left ridge is marked in crosses and for the right ridge in filled circles denoted in the same symbol as in the échelle diagram (left panel of Fig. 7)

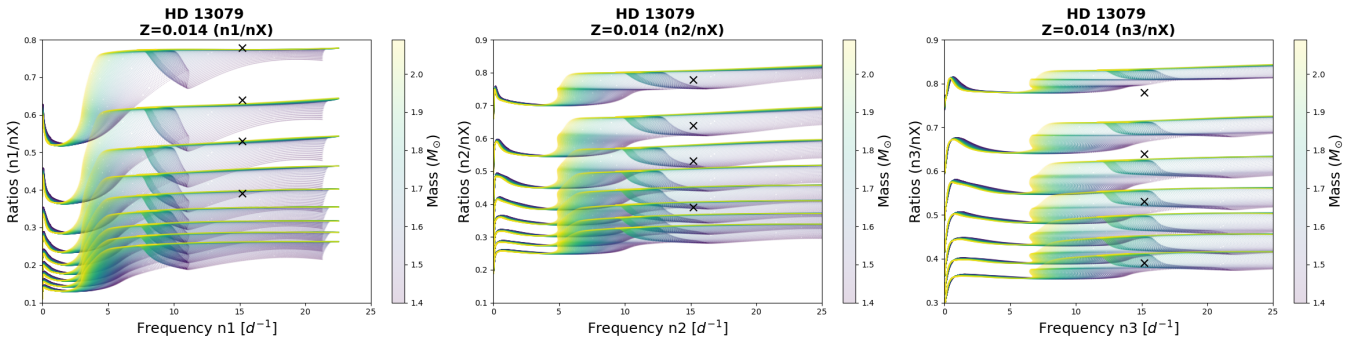

Figure A3. Frequency ratio diagrams (solid lines) calculated for HD 13079 with different masses (color coded) values in the range (1.40, 2.09) with solar metallicity $Z = 0.014$, $\alpha_{ov} = 0.1$ and $X_C < 0.745$. The different groups of lines correspond to increasing values of nX in the denominator from top to bottom, starting from $nX = 2$ (left), 3 (middle), and 4 (right). The crosses are corresponding to the frequency ratios calculated for *TESS* frequencies of HD 13079, marked as crosses in the échelle diagram (right panel of Fig. 7).

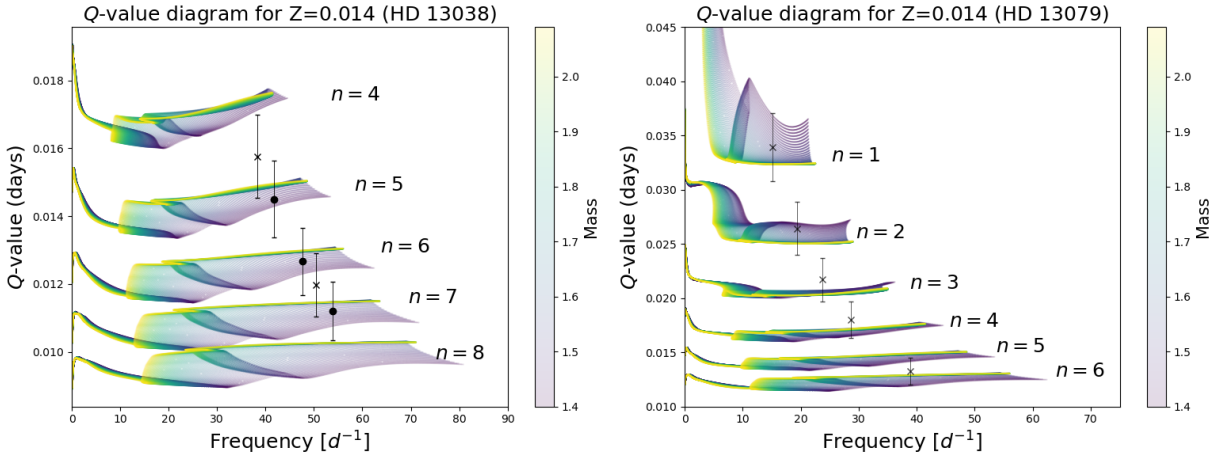

Figure A4. *Left:* Theoretical Q-values calculated for models with $Z = 0.014$ (solar metallicity) for $X_C < 0.745$. The Q-values for $n = 4$–8 with identified radial modes for HD 13038 are shown with cross errorbars. The blue circle errorbars represent the frequencies marked in crosses and circles in the échelle diagram in Fig. 7. In the right panel, the theoretical Q-values calculated for models with $Z = 0.014$ and $X_C < 0.745$ for $n = 1$–6 are also depicted. Q-values with identified radial modes for HD 13079 are shown as cross errorbars.

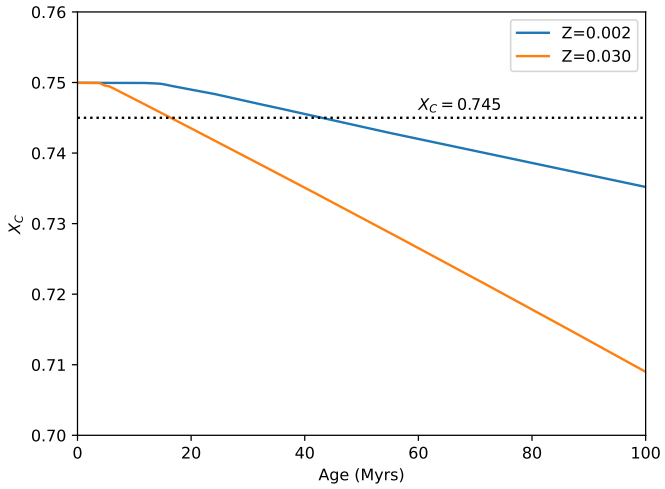

Figure A5. The diagram depicts the dependence of X_C on the age of the star are shown here for $Z = 0.002$ and $Z = 0.030$. The dotted line illustrates the level at which the core-H drops to 74.5%, at age between 20 Myrs to 35 Myrs for the models of metallicity range $Z = 0.002$ to 0.030 and is used as a starting point for the model calculation.

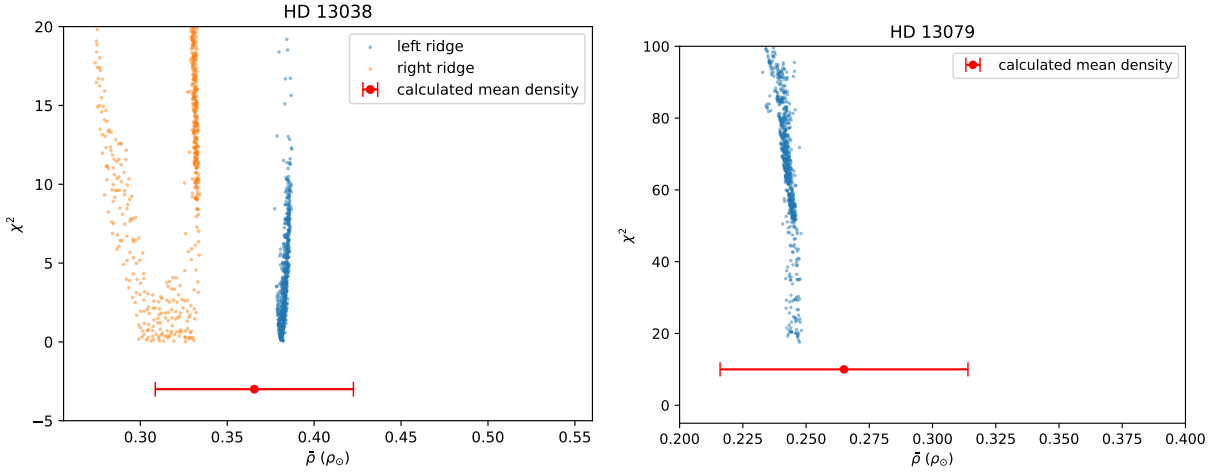

Figure A6. Left-panel: The diagram depicts the seismic-χ^2 vs $\bar{\rho}$ ($\rho_\odot$) for the stellar models with applied seismic constrained. The scattered points in orange are the models corresponding to the left-ridge frequencies for HD 13038 with modes $n = 5$ and 7. Similarly, the scattered points on the right in blue are the models corresponding to the right ridge with modes $n = 5, 6$ and 7, and the red errorbar is the range of calculated mean density. Right-panel: The same for the frequency ridge observed for HD 13079 for $n = 1, 2, 3, 4$ and 6.

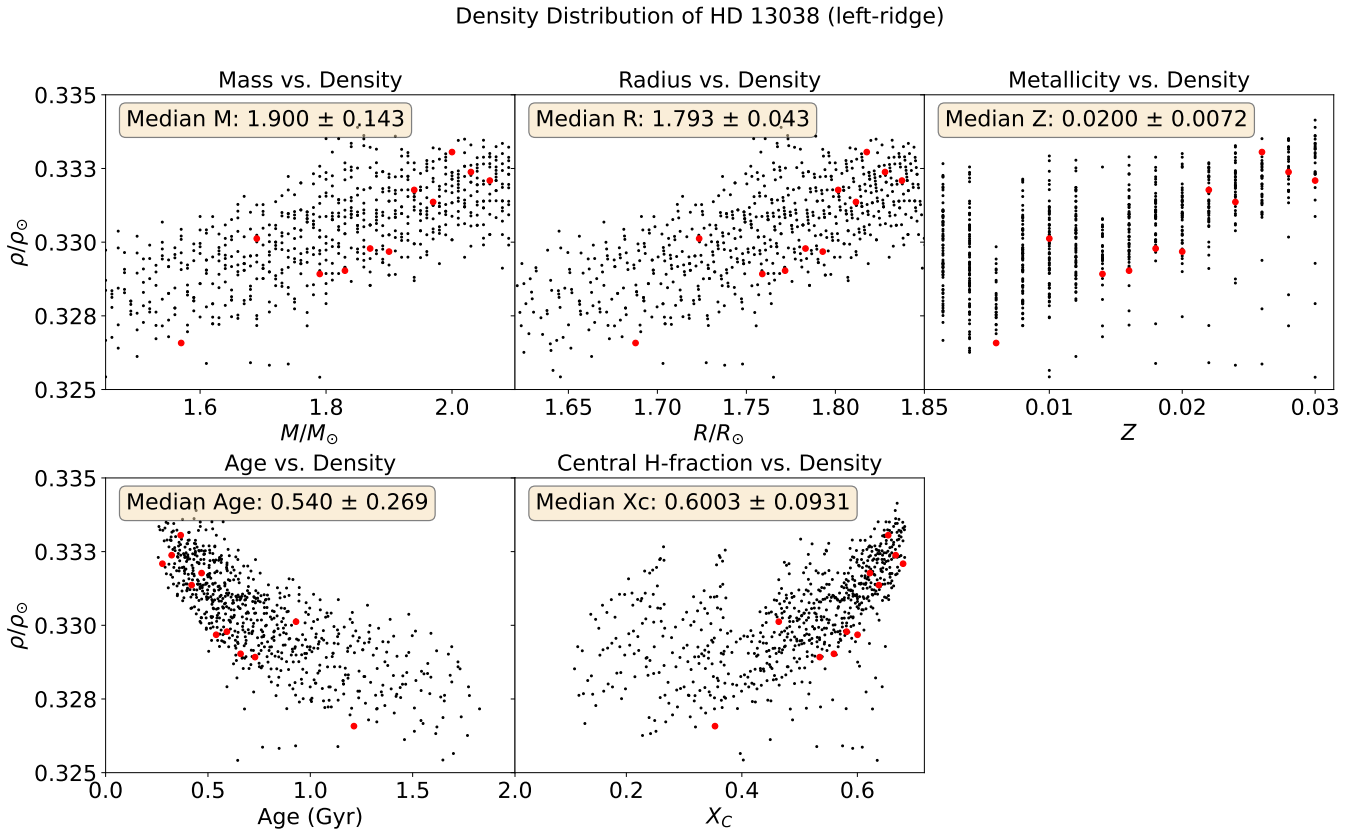

Figure A7. The plot shows the distribution of mean stellar density vs mass, radius, metallicity, age, X_C for the star HD 13038 corresponding to the left-ridge frequencies with $n = 5$ and 7 considered as radial modes. The black scatters correspond to the stellar model satisfying the least χ^2 value of each (M, Z) grid, and red points are the points corresponding to the stellar models among them that are located in the $1 - \sigma$ position in the H-R diagram, the median of which are considered as the best-fit parameters.

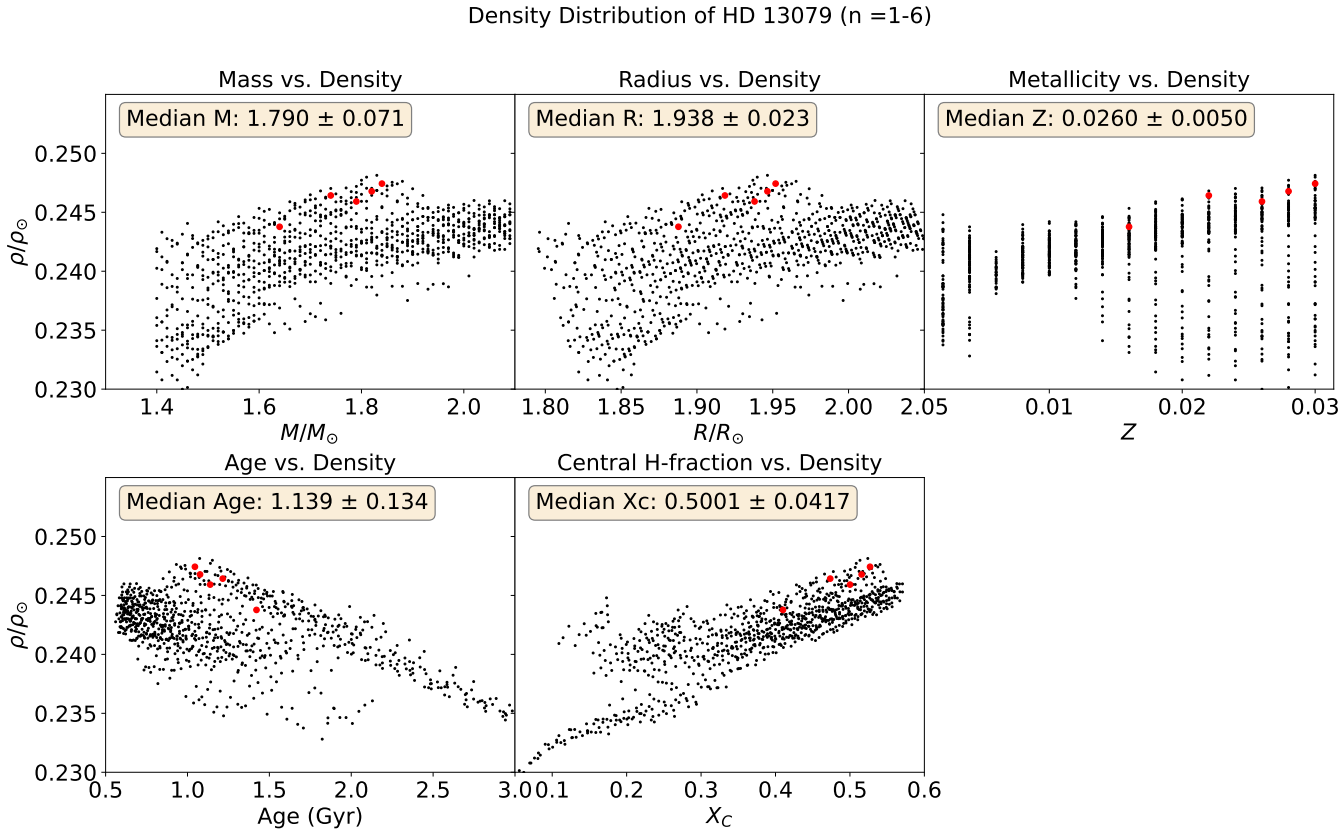

Figure A8. The plot displays the distribution of mean stellar density versus mass, radius, metallicity, age, and X_C for radial orders $n = 1, 2, 3, 4, 6$ for HD 13079. The black points represent stellar models with the least-χ^2 value for each (M, Z) grid element, while the red points indicate models that fall within the $1 - \sigma$ region of the H-R diagram. The median values of these red points define the best-fit stellar parameters.

Table A1. Frequencies and corresponding amplitudes, and phases for HD 13079 and HD 13079B obtained from the analysis of time-series observations from 1.3-m DFOT. The Rayleigh resolution of the time-series data used here is $\approx 6\ d^{-1}$.

ID	Frequency (d^{-1})	Amplitude (mag)	Phase	SNR
HD 13079				
f_1	19.06	0.0078	0.1702	5
HD 13079B				
f_1	8.7478	0.0037	0.0675	4
f_2	41.0475	0.0037	0.4759	4

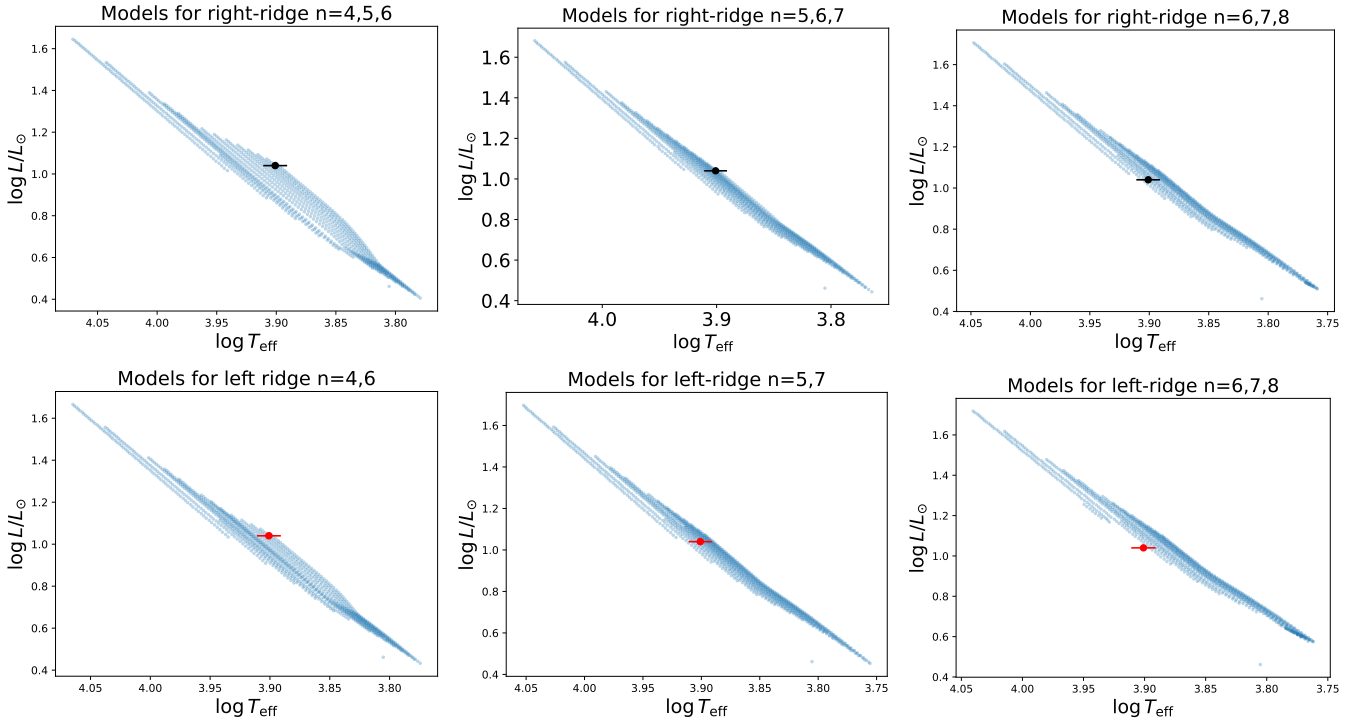

Figure A9. The models for HD 13038 were computed with $\alpha_{ov} = 0.1$ and $X_C < 0.745$, and the blue points indicate the models yielding the least-χ^2 values of each grid element (M, Z) for different combinations of consecutive radial overtones. The top-row panels show the models corresponding to the right-ridge frequencies, with the observed star marked by black error bars, for overtone triplets $(4, 5, 6)$, $(5, 6, 7)$ and $(6, 7, 8)$ from left to right. The bottom-row panels show the models corresponding to the left-ridge frequencies, with the observed star marked by red error bars, for overtone pairs $(4, 6)$, $(5, 7)$ and $(6, 8)$ from left to right.

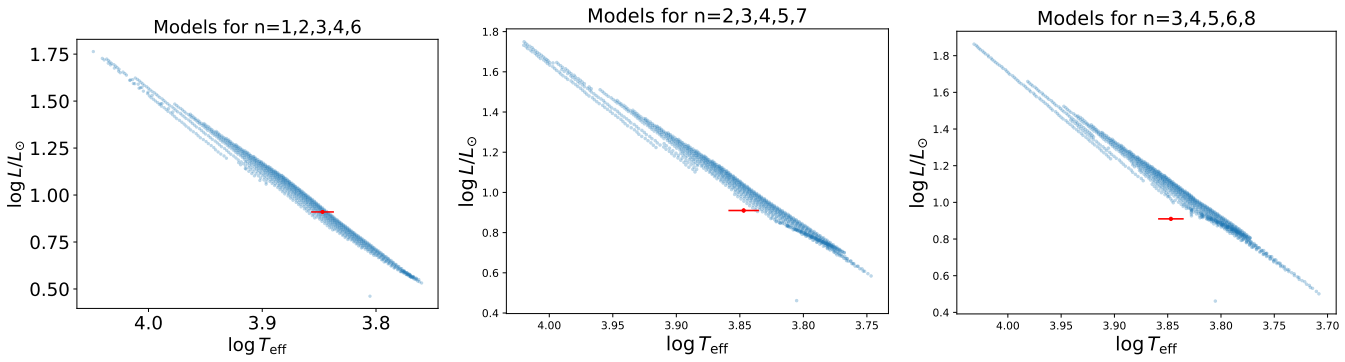

Figure A10. The blue scatters shown here represents the least-χ^2 models for HD 13079 for each of the grid for different combinations of consecutive radial overtones $(1, 2, 3, 4, 6)$, $(2, 3, 4, 5, 7)$ and $(3, 4, 5, 6, 8)$ for the frequencies $f_{69} = 15.18\ d^{-1}$, $f_1 = 19.41\ d^{-1}$, $f_{17} = 23.72\ d^{-1}$ and $f_{45} = 38.84\ d^{-1}$ that are marked in black cross on the right panel of Fig. 7. The red errorbar represents the location of the star HD 13079 on the H-R diagram.

Table A2. Extracted frequencies, amplitude and SNR for HD 13038 on utilizing *TESS* time-series data of sectors 58 (120 sec and 200 sec) and 85 (120 sec) in the order of decreasing amplitude. The mode identifications (n, ℓ, m) and Q-values are listed wherever applicable. The Rayleigh resolution of the time-series data for each sector $\approx 0.06\ d^{-1}$.

	Sector 58 (120 sec)			**Sector 58 (200 sec)**			**Sector 85 (120 sec)**					
ID	Frequency (d^{-1})	Amplitude (mmag)	SNR	Frequency (d^{-1})	Amplitude (mmag)	SNR	Frequency (d^{-1})	Amplitude (mmag)	SNR	(n, ℓ, m)	Q-values (days)	Comments
f_1	50.48	0.912	152.00	50.49	0.909	151.50	50.49	0.876	146.00	(7, 0, 0)	0.012 ± 0.001	$F7$
f_2	53.90	0.621	103.50	53.91	0.661	110.17	53.91	0.632	105.33			
f_3	47.71	0.515	85.83	47.71	0.505	84.17	47.72	0.530	88.33			
f_4	43.74	0.267	44.50	43.74	0.254	42.33	43.74	0.362	60.33			
f_5	50.72	0.176	29.33	50.72	0.181	30.17	50.73	0.183	30.50	–		
f_6	49.18	0.157	26.17	49.17	0.155	25.83	49.18	0.187	31.17			
f_7	0.47	0.145	24.17	0.47	0.168	28.00	0.47	0.280	46.67	–		
f_8	41.67	0.146	24.33	41.67	0.148	24.67	41.67	0.163	27.17			
f_9	42.26	0.140	23.33	42.26	0.138	23.00	42.26	0.114	19.00	-		
f_{10}	39.34	0.131	21.83	39.34	0.132	22.00	39.34	0.132	22.00	–		
f_{11}	40.97	0.126	21.00	40.97	0.124	20.67	40.97	0.104	17.33			
f_{12}	46.76	0.105	17.50	46.77	0.101	16.83	46.77	0.124	20.67			
f_{13}	45.33	0.099	15.15	45.34	0.102	17.00	–	–	–	–		
f_{14}	38.36	0.076	12.67	38.36	0.074	12.33	38.36	0.064	10.67			
f_{15}	51.26	0.075	12.50	51.26	0.063	10.50	–	–	–	–		
f_{16}	0.94	0.069	11.50	–	–	–	–	–	–	–		
f_{17}	47.94	0.069	11.50	47.95	0.071	11.83	–	–	–	–		
f_{18}	46.90	0.068	11.33	46.90	0.087	14.50	–	–	–	–		
f_{19}	43.93	0.064	10.67	43.93	0.089	14.83	–	–	–	–		
f_{20}	45.50	0.060	10.00	45.50	0.056	9.33	–	–	–	–		
f_{21}	48.53	0.049	8.17	48.53	0.048	8.00	–	–	–			
f_{22}	50.85	0.048	8.00	50.86	0.054	9.00	50.86	0.059	9.83	–		
f_{23}	47.52	0.048	8.00	47.52	0.048	8.00	–	–	–	–		
f_{24}	0.35	0.048	8.00	0.35	0.070	11.67	0.32	0.124	20.67	–		
f_{25}	54.99	0.046	7.67	54.99	0.046	7.67	–	–	–			
f_{26}	53.70	0.045	7.50	53.70	0.046	7.67	53.71	0.067	11.17	–		
f_{27}	52.53	0.043	7.17	52.53	0.045	7.50	–	–	–			
f_{28}	38.91	0.043	7.17	38.91	0.043	7.17	–	–	–			
f_{29}	50.99	0.042	7.00	50.99	0.041	6.83	–	–	–	–		
f_{30}	44.14	0.040	6.67	44.14	0.041	6.83	–	–	–	(5, 0, 0)	0.013 ± 0.001	$F5$
f_{31}	40.72	0.036	6.00	40.72	0.035	5.83	–	–	–			
f_{32}	33.44	0.028	5.02	–	–	–	–	–	–			
f_{33}	42.61	0.035	5.83	–	–	–	–	–	–			
f_{34}	–	–	–	0.59	0.082	13.67	–	–	–	–		
f_{35}	–	–	–	0.23	0.056	9.33	–	–	–	–		
f_{36}	–	–	–	0.71	0.043	7.17	–	–	–	–		
f_{37}	–	–	–	1.52	0.033	5.50	–	–	–	–		

Table A3. Extracted frequencies, amplitude and SNR for HD 13079 on utilizing *TESS* time-series data of sectors 18 (120 sec and 1800 sec) and 58 (200 sec). The mode identifications (n, ℓ, m) and Q-values are listed wherever applicable. The Rayleigh resolution of the time-series data for each sector $\approx 0.06\ d^{-1}$.

	Sector 18 (120 sec)			**Sector 18 (1800 sec)**			**Sector 58 (200 sec)**					
ID	Frequency (d^{-1})	Amplitude (mmag)	SNR	Frequency (d^{-1})	Amplitude (mmag)	SNR	Frequency (d^{-1})	Amplitude (mmag)	SNR	(n, ℓ,m)	Q-values (days)	Comments
f_1	19.41	5.390	539.0	19.41	4.110	411.0	19.41	5.423	542.3	(2, 0, −)	0.0265 ± 0.0025	$F2$
f_2	–	–	–	19.46	1.618	161.8	–	–	–	–		–
f_3	24.75	0.917	91.7	–	–	–	24.75	0.986	98.6			–
f_4	17.58	1.163	116.3	17.58	0.944	94.4	17.58	1.163	116.3	(1, 2, 0)		
f_5	9.52	0.814	81.4	9.52	0.768	76.8	9.52	0.224	22.4	–		
f_6	0.26	0.449	44.9	0.25	0.719	71.9	0.26	1.122	112.2	–		
f_7	18.33	0.791	79.1	–	–	–	18.33	0.805	80.5	(1, 2, +1)		
f_8	2.94	0.580	58.0	2.94	0.571	57.1	2.94	0.542	54.2	–		
f_9	8.26	0.554	55.4	8.26	0.539	53.9	8.26	0.294	29.4	–		–
f_{10}	–	–	–	8.15	0.535	53.5	–	–	–	–		
f_{11}	16.73	0.436	43.6	–	–	–	16.73	0.452	45.2	(1, 2, −1)		
f_{12}	–	–	–	0.37	0.725	72.5	–	–	–	–		–
f_{13}	–	–	–	0.30	0.646	64.6	–	–	–	–		–
f_{14}	5.46	0.309	30.9	–	–	–	–	–	–	–		–
f_{15}	7.42	0.296	29.6	7.43	0.287	28.7	7.42	0.133	13.3	–		–
f_{16}	18.82	0.399	39.9	18.83	0.295	29.5	18.82	0.373	30.0	(1, 2, +2)		
f_{17}	23.72	0.413	41.3	23.24	0.594	59.4	23.72	0.410	33.0	(3, 0, −)	0.0217 ± 0.0020	$F3$
f_{18}	1.01	0.181	18.1	1.01	0.329	32.9	1.01	0.157	15.7	–		–
f_{19}	–	–	–	0.49	0.332	33.2	–	–	–	–		
f_{20}	–	–	–	0.10	0.275	27.5	–	–	–	–		
f_{21}	20.03	0.318	31.8	–	–	–	20.03	0.313	25.0	–		–
f_{22}	1.80	0.250	25.0	1.78	0.214	21.4	1.80	0.123	12.3	–		–
f_{23}	1.86	0.176	17.6	1.86	0.197	19.7	1.86	0.247	24.7	–		–
f_{24}	–	–	–	1.09	0.274	27.4	–	–	–	–		–
f_{25}	2.17	0.232	23.2	2.16	0.265	26.5	2.17	0.376	37.6	–		–
f_{26}	2.24	0.210	21.0	2.25	0.173	17.3	2.24	0.112	11.2	–		–
f_{27}	7.26	0.160	16.0	7.27	0.183	18.3	7.26	0.219	21.9	–		
f_{28}	19.08	0.206	20.6	–	–	–	19.08	0.225	22.5			
f_{29}	15.83	0.195	19.5	–	–	–	15.83	0.161	16.1	(1, 2, −2)		–
f_{30}	–	–	–	2.04	0.118	11.8	–	–	–	–		
f_{31}	–	–	–	2.21	0.167	16.7	–	–	–	–		–
f_{32}	6.88	0.176	17.6	6.89	0.149	14.9	–	–	–	–		–
f_{33}	8.90	0.122	12.2	8.91	0.119	11.9	8.90	0.109	10.9	–		–
f_{34}	–	–	–	2.59	0.177	17.7	–	–	–	–		–
f_{35}	4.83	0.138	13.8	4.83	0.142	14.2	4.83	0.129	12.9	–		–
f_{36}	2.47	0.145	14.5	–	–	–	2.47	0.151	15.1	–		
f_{37}	1.30	0.146	14.6	–	–	–	1.30	0.177	17.7	–		
f_{38}	1.18	0.153	15.3	1.18	0.208	20.8	1.18	0.124	12.4	–		
f_{39}	8.53	0.151	15.1	–	–	–	–	–	–	–		–
f_{40}	37.27	0.138	13.8	–	–	–	37.27	0.140	14.0	-		
f_{41}	19.77	0.129	12.9	19.77	0.110	11.0	19.77	0.105	10.5	–		–
f_{42}	30.78	0.133	13.3	–	–	–	30.78	0.091	9.1			–
f_{43}	2.69	0.139	13.9	2.75	0.140	14.0	2.69	0.116	11.6	–		–
f_{44}	7.69	0.103	10.3	–	–	–	7.69	0.123	12.3	–		
f_{45}	38.84	0.119	11.9	–	–	–	38.84	0.108	10.8	(6, 0, 0)	0.01325 ± 0.00123	$F6$
f_{46}	8.75	0.126	12.6	8.75	0.121	12.1	8.75	0.109	10.9	–		
f_{48}	0.75	0.138	13.8	–	–	–	0.75	0.347	34.7	–		
f_{49}	–	–	–	22.16	0.123	12.3	–	–	–	–		
f_{50}	–	–	–	6.79	0.122	12.2	–	–	–	–		
f_{51}	–	–	–	6.20	0.108	10.8	–	–	–	–		
f_{52}	9.14	0.193	19.3	9.15	0.121	12.1	9.14	0.112	11.2	–		
f_{53}	–	–	–	2.78	0.107	10.7	2.79	0.116	11.6	–		
f_{54}	–	–	–	21.28	0.107	10.7	21.29	0.161	16.1	–		
f_{55}	–	–	–	6.58	0.114	11.4	–	–	–	–		
f_{56}	–	–	–	0.41	0.144	14.4	–	–	–	–		
f_{57}	–	–	–	8.10	0.116	11.6	–	–	–	–		
f_{58}	–	–	–	9.55	0.113	11.3	–	–	–	–		
f_{59}	–	–	–	7.46	0.116	11.6	–	–	–	–		
f_{60}	–	–	–	7.74	0.111	11.1	–	–	–	–		
f_{61}	–	–	–	1.21	0.155	15.5	–	–	–	–		
f_{62}	–	–	–	1.47	0.139	13.9	–	–	–	–		
f_{63}	–	–	–	1.30	0.134	13.4	–	–	–	–		
f_{64}	–	–	–	3.92	0.103	10.3	–	–	–	–		
f_{65}	17.92	0.160	16.0	17.87	0.102	10.2	17.92	0.185	18.5	–		
f_{66}	–	–	–	9.37	0.105	10.5	–	–	–	–		
f_{67}	–	–	–	2.53	0.122	12.2	–	–	–	–		
f_{68}	–	–	–	23.09	0.101	10.1	–	–	–	–		
f_{69}	15.18	0.100	0.458				–	–	–	(1, 0, −)	0.0339 ± 0.0031	$F1$

Table A4. Extracted frequencies ($\pm 0.054\ d^{-1}$) and corresponding amplitudes, phases, SNR, identified modes in terms of (n, ℓ, m) and Q-values calculated from the combined light curve for HD 13038.

Frequency (d^{-1})	Amplitude (mmag)	Phase	SNR	(n, ℓ, m)	Q-value (days)	Comments
f_1 = 50.493932	0.86	0.500	175.7	(7, 0, 0)	0.012 ± 0.001	$F7$
f_2 = 53.907784	0.62	0.522	126.2			
f_3 = 47.710296	0.50	0.540	100.7			
f_4 = 43.744411	0.29	0.042	59.6			
f_5 = 50.728256	0.15	0.500	37.8			
f_6 = 49.174138	0.16	0.500	33.2			
f_7 = 41.672648	0.15	0.795	31.1			
f_8 = 0.468026	0.15	0.500	30.2			
f_9 = 39.332925	0.13	0.175	25.8			
f_{10} = 42.266586	0.12	0.500	25.1			
f_{11} = 46.766253	0.11	0.858	22.5			
f_{12} = 40.980563	0.11	0.500	22.5			
f_{13} = 45.340321	0.10	0.245	20.7			
f_{14} = 46.898361	0.07	0.984	14.3			
f_{15} = 38.368897	0.07	0.500	14.2			
f_{16} = 51.272955	0.06	0.500	14.0			
f_{17} = 43.924535	0.07	0.796	13.6			
f_{18} = 47.956056	0.07	0.876	13.4			
f_{19} = 0.335948	0.06	0.026	13.0			
f_{20} = 50.594894	0.06	0.500	13.0			
f_{21} = 0.941969	0.06	0.123	12.2			
f_{22} = 0.189848	0.06	0.248	11.8			
f_{23} = 48.532123	0.05	0.993	10.5			
f_{24} = 45.502381	0.05	0.500	10.5			
f_{25} = 0.665849	0.05	0.500	10.1			
f_{26} = 50.865826	0.05	0.212	10.1			
f_{27} = 50.993937	0.05	0.280	10.2			
f_{28} = 53.711600	0.05	0.500	9.6			
f_{29} = 50.391731	0.06	0.500	9.6			
f_{30} = 52.527811	0.04	0.500	9.1			
f_{31} = 55.003582	0.04	0.477	9.0			
f_{32} = 44.142414	0.04	0.841	8.8	(5, 0, 0)	0.013 ± 0.001	$F5$
f_{33} = 0.013926	0.10	0.402	8.4			
f_{34} = 38.902920	0.04	0.500	8.1			
f_{35} = 47.520224	0.04	0.203	7.4			
f_{36} = 0.819915	0.04	0.153	7.3			
f_{37} = 40.736670	0.03	0.447	6.7			
f_{38} = 43.608590	0.03	0.705	6.6			
f_{39} = 1.443813	0.03	0.837	6.0			
f_{40} = 1.617865	0.03	0.044	5.9			
f_{41} = 42.622687	0.03	0.947	5.8			
f_{42} = 46.510392	0.03	0.070	5.8			
f_{43} = 5.079601	0.03	0.787	5.6			
f_{44} = 1.285878	0.03	0.110	5.6			
f_{45} = 50.245868	0.03	0.976	5.3			
f_{46} = 47.820367	0.03	0.736	5.2			
f_{47} = 33.445154	0.03	0.477	5.1			
f_{48} = 2.159861	0.02	0.848	5.1			
f_{49} = 48.080078	0.02	0.058	5.0			

Table A5. Extracted frequencies (±0.0013 d^{-1}) and corresponding amplitudes, phases, SNR, identified modes in terms of (n, ℓ, m) and Q-values calculated from the combined light curve for HD 13079.

Frequency (d^{-1})	Amplitude (mmag)	Phase	SNR	(n, ℓ, m)	Q (days)	Comments
f_1 = 19.404407	5.41	0.074	648.7	(2, 0, −)	0.0265 ± 0.0025	
f_2 = 17.584593	1.14	0.067	151.7	(1, 1, 0)		
f_3 = 24.750064	0.90	0.711	120.0			
f_4 = 18.338478	0.83	0.988	109.9	(1, 1, +1)		
f_5 = 19.506488	0.74	0.375	98.1			
f_6 = 0.252045	0.64	0.775	83.1			
f_7 = 0.122044	0.64	0.200	84.5			
f_8 = 2.937792	0.56	0.691	75.8			
f_9 = 9.521294	0.55	0.774	74.2			
f_{10} = 16.736723	0.44	0.965	58.8	(1, 1, −1)		
f_{11} = 23.726170	0.42	0.895	55.4	(3, 0, −)	0.0217 ± 0.0020	
f_{12} = 18.820541	0.41	0.285	54.7	(1, 1, +2)		
f_{13} = 8.259406	0.40	0.269	53.1			
f_{14} = 19.252496	0.33	0.032	45.3			
f_{15} = 19.654484	0.33	0.703	44.5			
f_{16} = 8.149323	0.32	0.585	43.9			
f_{17} = 20.025498	0.27	0.071	37.9			
f_{18} = 2.177872	0.28	0.026	37.3			
f_{19} = 19.080422	0.25	0.024	33.7			
f_{20} = 0.381969	0.23	0.901	32.0			
f_{21} = 0.711930	0.23	0.505	31.5			
f_{22} = 7.429346	0.22	0.106	30.1			
f_{23} = 5.457569	0.21	0.104	29.1			
f_{24} = 25.844014	0.21	0.536	27.6			
f_{25} = 24.895975	0.20	0.684	27.6			
f_{26} = 7.265499	0.20	0.717	26.4			
f_{27} = 15.828745	0.18	0.443	24.9	(1, 1, −2)		
f_{28} = 17.928521	0.17	0.052	23.9			
f_{29} = 21.292230	0.17	0.375	23.1			
f_{30} = 0.857937	0.15	0.725	21.3			
f_{31} = 1.781249	0.14	0.839	21.2			
f_{32} = 2.469803	0.15	0.288	20.6			
f_{33} = 1.085855	0.15	0.356	20.2			
f_{34} = 18.950477	0.14	0.850	20.2			
f_{35} = 19.756397	0.14	0.138	19.8			
f_{36} = 37.271058	0.14	0.661	19.4			
f_{37} = 1.239908	0.14	0.362	19.0			
f_{38} = 9.137300	0.13	0.250	18.0			
f_{39} = 4.839634	0.13	0.893	17.9			
f_{40} = 15.940706	0.12	0.668	17.7			
f_{41} = 0.587994	0.12	0.705	17.6			
f_{42} = 38.818883	0.12	0.175	17.5			
f_{43} = 19.872438	0.12	0.362	17.5			
f_{44} = 6.945486	0.12	0.001	16.8			
f_{45} = 2.582778	0.12	0.665	15.9			
f_{46} = 30.777606	0.11	0.681	15.3			
f_{47} = 7.533428	0.11	0.001	15.3			
f_{48} = 8.745291	0.11	0.686	15.0			
f_{49} = 8.541388	0.11	0.219	15.1			
f_{50} = 3.729731	0.10	0.275	14.8			
f_{51} = 2.801827	0.10	0.158	14.7			
f_{52} = 20.240396	0.10	0.657	14.5			
f_{53} = 1.369820	0.10	0.191	14.5			
f_{54} = 7.694319	0.09	0.500	13.9			
f_{55} = 7.859411	0.09	0.060	13.4			
f_{56} = 1.889855	0.09	0.013	13.2			
f_{57} = 9.391218	0.09	0.632	13.0			
f_{58} = 6.781374	0.09	0.282	12.9			
f_{59} = 8.911244	0.09	0.130	12.7			
f_{60} = 6.573447	0.09	0.236	12.7			

Frequency (d^{-1})	Amplitude (mmag)	Phase	SNR	(n, ℓ, m)	Q (days)	Comments
f_{61} = 2.691756	0.09	0.600	12.6			
f_{62} = 0.026051	0.08	0.254	12.4			
f_{63} = 2.041793	0.09	0.485	12.0			
f_{64} = 9.665244	0.08	0.748	11.9			
f_{65} = 6.201492	0.08	0.831	11.9			
f_{66} = 9.015229	0.09	0.755	12.0			
f_{67} = 9.925257	0.08	0.179	11.5			
f_{68} = 18.568472	0.08	0.748	10.9			
f_{69} = 10.957169	0.08	0.652	10.9			
f_{70} = 25.415949	0.07	0.970	10.5			
f_{71} = 8.021409	0.07	0.080	10.5			
f_{72} = 9.245326	0.08	0.217	10.4			
f_{73} = 18.128597	0.07	0.957	10.4			
f_{74} = 1.503796	0.07	0.859	10.2			
f_{75} = 8.371391	0.07	0.944	10.1			
f_{76} = 18.670450	0.07	0.960	10.0			
f_{77} = 76.607904	0.07	0.237	9.5			
f_{78} = 0.959935	0.07	0.088	9.4			
f_{79} = 10.406262	0.06	0.136	9.3			
f_{80} = 20.126342	0.07	0.783	9.2			
f_{81} = 22.342265	0.06	0.178	9.0			
f_{82} = 28.609639	0.06	0.850	8.9	$(4, 0, -)$	0.0180 ± 0.0016	
f_{83} = 15.206847	0.06	0.599	8.5	$(1, 0, -)$	0.0339 ± 0.0031	
f_{84} = 3.921695	0.06	0.778	8.3			
f_{85} = 1.604797	0.06	0.866	8.2			
f_{86} = 14.002797	0.06	0.970	8.2			
f_{87} = 17.826646	0.06	0.553	8.1			
f_{88} = 67.392637	0.06	0.008	7.9			
f_{89} = 3.051810	0.06	0.339	7.8			
f_{90} = 2.307910	0.06	0.033	7.8			
f_{91} = 20.344353	0.06	0.437	7.8			
f_{92} = 20.500375	0.05	0.206	7.6			
f_{93} = 17.422615	0.05	0.020	7.5			
f_{94} = 9.787258	0.05	0.500	7.5			
f_{95} = 20.840326	0.05	0.234	7.5			
f_{96} = 17.048657	0.05	0.500	7.3			
f_{97} = 6.355493	0.05	0.983	7.1			
f_{98} = 11.251097	0.05	0.214	7.1			
f_{99} = 11.594906	0.05	0.134	7.1			
f_{100} = 7.105466	0.05	0.571	7.0			
f_{101} = 3.227824	0.05	0.808	7.0			
f_{102} = 20.680336	0.05	0.494	6.9			
f_{103} = 10.245149	0.05	0.225	6.9			
f_{104} = 17.718636	0.05	0.563	6.8			
f_{105} = 6.675465	0.05	0.107	6.6			
f_{106} = 10.605136	0.05	0.556	6.5			
f_{107} = 38.850849	0.05	0.780	6.4	$(6, 0, -)$	0.0132 ± 0.0012	
f_{108} = 5.785595	0.05	0.305	6.4			
f_{109} = 5.679508	0.05	0.356	6.4			
f_{110} = 21.056346	0.04	0.372	6.4			
f_{111} = 10.705147	0.04	0.166	6.3			
f_{112} = 6.047498	0.04	0.246	6.2			
f_{113} = 10.853085	0.04	0.770	6.2			
f_{114} = 6.467429	0.04	0.675	6.1			
f_{115} = 5.251613	0.04	0.848	6.1			
f_{116} = 18.230374	0.05	0.500	6.0			
f_{117} = 12.249006	0.04	0.652	6.0			
f_{118} = 11.405026	0.04	0.477	5.5			
f_{119} = 11.848980	0.04	0.739	5.6			
f_{120} = 24.633973	0.04	0.500	5.5			
f_{121} = 44.164504	0.04	0.007	5.5			
f_{122} = 23.308120	0.04	0.481	5.5			
f_{123} = 5.933492	0.04	0.347	5.4			

Frequency (d^{-1})	Amplitude (mmag)	Phase	SNR	(n, ℓ, m)	Q-value (days)	Comments
f_{124} = 21.932265	0.04	0.103	5.3			
f_{125} = 3.359740	0.04	0.690	5.3			
f_{126} = 3.471719	0.04	0.097	5.4			
f_{127} = 4.433666	0.04	0.600	5.3			
f_{128} = 10.141106	0.04	0.046	5.2			
f_{129} = 21.560348	0.04	0.642	5.1			
f_{130} = 21.422266	0.03	0.542	5.3			
f_{131} = 17.196686	0.04	0.755	5.1			
f_{132} = 16.340649	0.04	0.303	5.3			
f_{133} = 48.268110	0.04	0.391	5.1			
f_{134} = 5.563517	0.04	0.500	5.0			